



HAL
open science

Magnetic field, activity, and companions of V410 Tau

Louise Yu, J.-F. Donati, K. Grankin, A. Collier Cameron, C. Moutou, G. Hussain, C. Baruteau, L. Jouve

► **To cite this version:**

Louise Yu, J.-F. Donati, K. Grankin, A. Collier Cameron, C. Moutou, et al.. Magnetic field, activity, and companions of V410 Tau. *Monthly Notices of the Royal Astronomical Society: Letters*, 2019, 489 (4), pp.5556-5572. 10.1093/mnras/stz2481 . hal-03024308

HAL Id: hal-03024308

<https://cnrs.hal.science/hal-03024308>

Submitted on 22 May 2023

HAL is a multi-disciplinary open access archive for the deposit and dissemination of scientific research documents, whether they are published or not. The documents may come from teaching and research institutions in France or abroad, or from public or private research centers.

L'archive ouverte pluridisciplinaire **HAL**, est destinée au dépôt et à la diffusion de documents scientifiques de niveau recherche, publiés ou non, émanant des établissements d'enseignement et de recherche français ou étrangers, des laboratoires publics ou privés.

Magnetic field, activity, and companions of V410 Tau

L. Yu,^{1★} J.-F. Donati,¹ K. Grankin,² A. Collier Cameron,³ C. Moutou,⁴ G. Hussain,^{1,5}
C. Baruteau,¹ L. Jouve¹ and the MaTYSSSE collaboration

¹Univ. de Toulouse, CNRS, IRAP, 14 Avenue E. Belin, F-31400 Toulouse, France

²Crimean Astrophysical Observatory, 298409 Nauchny, Crimea

³SUPA, School of Physics & Astronomy, University of St Andrews, St Andrews, Scotland KY16 9SS, UK

⁴CFHT Corporation, 65-1238 Mamalahoa Hwy, Kamuela, HI 96743, USA

⁵ESO, Karl-Schwarzschild-Str 2, D-85748 Garching, Germany

Accepted 2019 September 3. Received 2019 August 28; in original form 2019 July 11

ABSTRACT

We report the analysis, conducted as part of the MaTYSSSE programme, of a spectropolarimetric monitoring of the ~ 0.8 Myr, $\sim 1.4 M_{\odot}$ disc-less weak-line T Tauri star V410 Tau with the ESPaDOnS instrument at the Canada–France–Hawaii Telescope and NARVAL at the T el escope Bernard Lyot, between 2008 and 2016. With Zeeman–Doppler Imaging, we reconstruct the surface brightness and magnetic field of V410 Tau, and show that the star is heavily spotted and possesses a ~ 550 G relatively toroidal magnetic field. We find that V410 Tau features a weak level of surface differential rotation between the equator and pole ~ 5 times weaker than the solar differential rotation. The spectropolarimetric data exhibit intrinsic variability, beyond differential rotation, which points towards a dynamo-generated field rather than a fossil field. Long-term variations in the photometric data suggest that spots appear at increasing latitudes over the span of our data set, implying that, if V410 Tau has a magnetic cycle, it would have a period of more than 8 yr. Having derived raw radial velocities (RVs) from our spectra, we filter out the stellar activity jitter, modelled either from our Doppler maps or using Gaussian process regression. Thus filtered, our RVs exclude the presence of a hot Jupiter-mass companion below ~ 0.1 au, which is suggestive that hot Jupiter formation may be inhibited by the early depletion of the circumstellar disc, which for V410 Tau may have been caused by the close (few tens of au) M dwarf stellar companion.

Key words: magnetic fields – techniques: polarimetric – stars: imaging – stars: individual: V410 Tau – stars: rotation.

1 INTRODUCTION

Investigating the birth and youth of low-mass stars ($< 3 M_{\odot}$) and of their planetary systems heavily contributes to unveiling the origin and history of the Sun and of its planets, in particular the life-hosting Earth. We know that stars and their planets form from the collapse of parsec-sized molecular clouds which progressively flatten into massive accretion discs, until finally settling as pre-main-sequence (PMS) stars surrounded by protoplanetary discs. T Tauri stars (TTs) are PMS stars that have emerged from their dust cocoons and are gravitationally contracting towards the main sequence (MS); typically aged 1–15 Myr, they are classical TTs (cTTs) when they are still surrounded by a massive accretion disc (where planets are potentially forming), and weak-line TTs (wTTs) when their

accretion has stopped and their inner disc has dissipated. Large-scale magnetic fields are known to play a crucial role in the early life of low-mass stars, as they can open a magnetospheric gap at the centre of the disc, funnel accreting disc material on to the star, induce stellar winds and prominences, and thus impact the angular momentum evolution of TTs (Donati & Landstreet 2009). Observing and understanding the magnetic topologies of TTs is therefore a necessary endeavour to complete our understanding of stellar and planetary formation (e.g. Bouvier et al. 2007).

Since the first detection of a magnetic field around a cTTs nearly 20 yr ago (Johns-Krull, Valenti & Koresko 1999), the large-scale topologies of a dozen cTTs were mapped (e.g. Donati et al. 2007; Hussain et al. 2009; Donati et al. 2010a, 2013) thanks to the MaPP (Magnetic Protostars and Planets) Large Observing Programme allocated on the 3.6 m Canada–France–Hawaii Telescope (CFHT) with the ESPaDOnS (Echelle SpectroPolarimetric Device for the

* E-mail: louise.yu@irap.omp.eu

Observation of Stars) high-resolution spectropolarimeter, using Zeeman-Doppler Imaging (ZDI), a tomography technique designed for imaging the brightness features and magnetic topologies at the surfaces of active stars (e.g. Donati & Brown 1997). This first exploration showed that the topologies of cTTSs are either quite simple or rather complex depending on whether the stars are fully convective or largely radiative, respectively (Gregory et al. 2012; Donati et al. 2013). Moreover, these fields are reported to vary with time (e.g. Donati et al. 2011, 2012, 2013) and resemble those of mature stars with similar internal structure (e.g. Morin et al. 2008), suggesting that they are produced through dynamo processes within the bulk of the convective zone.

The MaTYSSSE (Magnetic Topologies of Young Stars and the Survival of close-in giant Exoplanets) Large Programme aims at mapping the large-scale magnetic topologies of ~ 35 wTTSs, comparing them to those of cTTSs and MS stars, and probing the potential presence of massive close-in exoplanets (hot Jupiters/hJs) around its targets. It was allocated at CFHT over semesters 2013a to 2016b (510 h) with complementary observations from the ESPaDOnS twin NARVAL on the T telescop e Bernard Lyot (TBL) at Pic du Midi in France and from the HARPS spectropolarimeter at the ESO Telescope at La Silla in Chile. Up to now, about a dozen wTTSs were studied with MaTYSSSE for their magnetic topologies and activity, for example V410 Tau (Skelly et al. 2010), LkCa 4 (Donati et al. 2014), and V830 Tau (Donati et al. 2017). These studies showed that the fields of wTTSs are much more diverse than those of cTTSs, with for example V410 Tau and LkCa 4 displaying strong toroidal components despite being fully convective, as opposed to the results obtained on cTTSs (see discussion in Donati et al. 2014). MaTYSSSE fostered the detection of two hJs around wTTSs, the 2 Myr-old V830 Tau b (Donati et al. 2016, 2017) and the 17 Myr-old TAP 26 b (Yu et al. 2017).

This new study focuses on V410 Tau, a very young (~ 1 Myr in Skelly et al. 2010) disc-less wTTS (Luhman et al. 2010) with a well-constrained rotation period of 1.872 d (Stelzer et al. 2003). One of the most observed wTTSs, V410 Tau has been the target of both photometric and spectropolarimetric observation campaigns. High variability detected in its light curve (Bouvier & Bertout 1989; Grankin et al. 2008; Sokoloff et al. 2008) indicates a high level of activity, confirmed with Doppler maps (Skelly et al. 2010; Rice, Strassmeier & Kopf 2011; Carroll et al. 2012) showing that the photosphere features large polar and equatorial cool spots, responsible for these modulations. Magnetic maps made by Skelly et al. (2010) and Carroll et al. (2012) have shown a highly toroidal and non-axisymmetric large-scale field despite the mostly convective structure of V410 Tau.

We first describe our data, comprising new NARVAL data from MaTYSSSE added to previous spectropolarimetric data taken with ESPaDOnS and NARVAL in 2008–2011, and contemporaneous photometric observations taken at the Crimean Astronomical Observatory (CrAO) and from the Super Wide Angle Search for Planets (SuperWASP) campaign (Section 2). We then derive the general properties of V410 Tau (Section 3), after which we pursue the investigation of both its photosphere and its magnetic field, using ZDI with a model including both bright plagues and cool spots (Section 4). Then, we disentangle the activity jitter from the actual radial velocities (RVs) in the RV curve, using models from our ZDI maps and Gaussian process regression (GPR), in order to look for a potential planet signature (Section 5), before finally discussing our results and concluding (Section 6).

2 OBSERVATIONS

Our spectropolarimetric data set spans from 2008 October to 2016 January, totalling 144 high-resolution optical spectra, both unpolarized (Stokes I) and circularly polarized (Stokes V). It is composed of eight runs, most of which cover around 15 d, taken during four different seasons: 2008b–2009a, 2011a, 2013b, and 2015b–2016a. The full journal of observations is available in Table A1. The 2008b data set and four points in the 2009a data set were taken with the ESPaDOnS echelle spectropolarimeter at CFHT, while the rest were taken with the ESPaDOnS twin NARVAL installed at TBL.

The raw frames are processed with the nominal reduction package LIBRE ESPRIT as described in e.g. Donati et al. (1997, 2011), yielding a typical root-mean-square (rms) RV precision of 20–30 m s^{-1} (Moutou et al. 2007; Donati et al. 2008). The peak signal-to-noise ratios (S/N, per 2.6 km s^{-1} velocity bin) reached on the spectra range between 82 and 238 for the majority (three spectra have an S/N lower than 70 and were rejected for ZDI and the RV analysis), with a median of 140.

Time is counted in units of stellar rotation, using the same reference date and rotation period as in Skelly et al. (2010), namely $\text{BJD}_0 = 2454832.58033$ and $P_{\text{rot}} = 1.871970 \pm 0.000010$ d (Stelzer et al. 2003), respectively:

$$c = (\text{BJD} - \text{BJD}_0) / P_{\text{rot}}. \quad (1)$$

The stellar phase is defined as the decimal part of the cycle c .

The emission core of the Ca II infrared triplet (IRT) presents an average equivalent width (EW) of $\simeq 13 \text{ km s}^{-1}$ (0.37 \AA). The He I D_3 line is relatively weak with an average EW of 13 km s^{-1} as well (0.25 \AA), in agreement with the non-accreting status of V410 Tau. The H α line has an average EW of 14 km s^{-1} (0.33 \AA) and an rms EW of 27 km s^{-1} and exhibits a periodicity of period 1.8720 ± 0.0009 d (see Appendix C, available online). From the He I D_3 line, we detected small flares on 2008 December 10 (rotational cycle $-15+3.514$, as per Table A1), on the night of 2013 December 8 to 2013 December 9 (rotational cycles $959+4.090$ and $959+4.151$), and on the night of 2016 January 20 (rotational cycles $1376+0.021$ and $1376+0.040$). One big flare, on 2008 December 15 (rotational cycle $-15+6.181$), was visible not only in He I D_3 (EW $\simeq 30 \text{ km s}^{-1}$) but also in H α (EW $\simeq 230 \text{ km s}^{-1}$) and the Ca II IRT (core emission EW $\simeq 40 \text{ km s}^{-1}$). We removed the six flare-subjected observations from our data sets in order to proceed with the mapping of the photosphere and surface magnetic field, as well as the RV analysis.

Least-squares deconvolution (LSD; see Donati et al. 1997) was applied to all our spectra in order to add up information from all spectral lines and boost the resulting S/N of both Stokes I and VLSD profiles. The spectral mask we employed for LSD was computed from an ATLAS9 LTE model atmosphere (Kurucz 1993) featuring $T_{\text{eff}} = 4500$ K and $\log g = 3.5$, and involves about 7800 spectral features (with about 40 per cent from Fe I, see e.g. Donati et al. 2010b, for more details). Stokes I and Stokes V LSD profiles shown in Section 4 display distortions that betray the stellar activity with a periodicity corresponding to the rotation of the star. Moonlight pollution, which affects 15 of our Stokes I LSD profiles, was filtered out using a two-step tomographic imaging process described in Donati et al. (2016). The S/N in the Stokes I LSD profiles, ranging from 1633 to 2930 (per 1.8 km s^{-1} velocity bin) with a median of 2410, is measured from continuum intervals, including not only the noise from photon statistics, but also the (often dominant) noise introduced by LSD (see Table A1). The S/N in Stokes V LSD

profiles, dominated by photon statistics, range from 1817 to 6970 with a median value of 3584.

Phase coverage is of varying quality depending on the observation epoch. The 2008b data set, with only six points, covers only half the surface of the star (phases -0.20 to 0.30). The 2009a data set, although the densest with 48 points in 16 d and including data from both instruments, lacks observations between phases 0.05 and 0.20 . The 2011a data set presents a large gap between phases -0.05 and 0.15 , and a smaller one between phases 0.65 and 0.80 . The 2013b and 2015b data sets are well sampled, and the 2016a data set, with only nine points, lacks observations between phases 0.25 to 0.45 and -0.15 to 0.05 .

Contemporaneous BVR_I photometric measurements, documented in Table A2, were taken from the Crimean Astrophysical Observatory 1.25 and 0.60 m telescopes between 2008 August and 2017 March, counting 420 observations distributed over nine runs at a rate of one run per year, each run covering 3–7 months. In each run, the visible magnitude presents modulations of a period ~ 1.87 d and amplitude varying from 0.04 to 0.24 mag (see Appendix B, available online). The visible magnitude reaches a global minimum of 10.563 during the 2014b run. We also used 2703 data points of visible magnitude from the Wide Angle Search for Planets (WASP; Pollacco et al. 2006) photometric campaign covering semesters 2010b–2011a. Plots of the photometric data contemporaneous to our spectropolarimetric runs (i.e. 2008b + 2009a, 2010b + 2011a, 2013b + 2014a, and 2015b + 2016a) are visible in Section 4.

3 EVOLUTIONARY STATUS OF V410 TAU

V410 Tau is a very well-observed three-star system located in the Taurus constellation at $d = 129.0 \pm 0.5$ pc from Earth (Galli et al. 2018, we chose this value over the *Gaia* result, 130.4 ± 0.9 pc, because it is both in agreement with it and more precise). V410 Tau B was estimated to have a mass 0.2 ± 0.1 times that of V410 Tau A, and V410 Tau C to have a mass $0.08^{+0.10}_{-0.08}$ times that of V410 Tau AB (Kraus et al. 2011). The sky-projected separation between V410 Tau A and V410 Tau B was measured at 0.13 ± 0.01 arcsec, i.e. 16.8 ± 1.4 au, and that between V410 Tau AB and V410 Tau C was measured at 0.28 ± 0.01 arcsec, i.e. 36 ± 3 au. Given that V410 Tau A is much brighter than V410 Tau B and V410 Tau C in the optical bandwidth (Ghez, White & Simon 1997), we consider that the spectra analysed in this study characterize the light of V410 Tau A predominantly. Applying the automatic spectral classification tool developed within the frame of the MaPP and MaTYSSE projects (Donati et al. 2012), we constrain the temperature and logarithmic gravity of V410 Tau A to, respectively, $T_{\text{eff}} = 4500 \pm 100$ K and $\log g = 3.8 \pm 0.2$.

Its rotation period was previously estimated to $P_{\text{rot}} = 1.871970 \pm 0.000010$ d (Stelzer et al. 2003), a value which we use throughout this paper to phase our data (see equation 1). Comparing both our contemporary measurements (Table A2) and those found in Grankin et al. (2008), we find that the minimum magnitude measured on V410 Tau is 10.52 ± 0.02 , value that we use as a reference to compute the unspotted magnitude.

Our photometric measurements yield a mean $B - V$ index of 1.17 ± 0.02 , and since the theoretical $B - V$ at 4500 K is 1.04 ± 0.02 (Pecaut & Mamajek 2013; Table 6), the amount of visual extinction is $A_V = 3.1 \times (1.17 - 1.04) = 0.40 \pm 0.10$. The bolometric correction at T_{eff} being equal to -0.64 ± 0.05 (Pecaut & Mamajek 2013; Table 6), and the distance modulus to $-5 \times \log_{10}(d/10) = -5.55 \pm 0.01$, we find an absolute magnitude of 3.93 ± 0.11 .

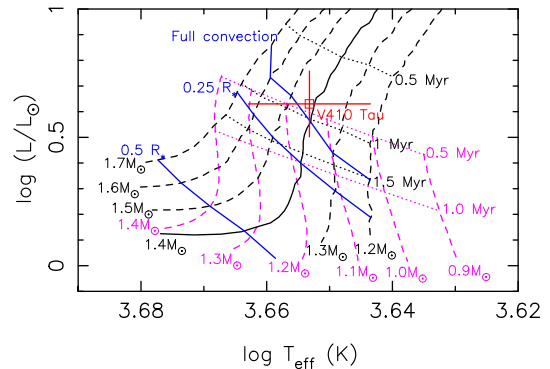


Figure 1. Position of V410 Tau (red) in the Hertzsprung–Russell diagram. The curves yielded by the Siess models (with solar metallicity and overshooting) are represented in black and those yielded by the Baraffe models are represented in magenta. In both cases, evolution tracks are displayed in dashed lines, except the Siess $1.4 M_{\odot}$ track, the one we chose to model the evolution of V410 Tau, which is shown as a full line. Isochrones are displayed in dotted lines. The thresholds where the radiative core starts developing (‘Full convection’) and where it reaches 25 per cent of the stellar radius, according to the Siess models, are marked in blue.

The value of $v \sin i^1$ found from the spectra, $73.2 \pm 0.2 \text{ km s}^{-1}$ (see Section 4), indicates that the minimum radius of the star $R_{*} \sin i$ is equal to $2.708 \pm 0.007 R_{\odot}$, which implies a maximum absolute unspotted magnitude of 3.67 ± 0.10 given the photospheric temperature. The discrepancy with the value found in the previous paragraph indicates the presence of dark spots on the photosphere even when the star is the brightest. If we assume a spot coverage at maximum brightness of ~ 25 per cent, typical of active stars, (like it was done in Donati et al. 2014, 2015; Yu et al. 2017), then the unspotted absolute magnitude would be 3.61 ± 0.32 , which corresponds to an inclination² of $77 \pm 22^{\circ}$. However, the models best fitting our spectra have an inclination of $50 \pm 10^{\circ}$ (see Section 4), which would require the spot coverage at maximum brightness to actually be ~ 50 per cent. Such a high permanent spot coverage is unusual but not unconceivable, since another wTTS, LkCa4, was observed to have as much as 80 per cent of its surface covered with spots (Gully-Santiago et al. 2017). Assuming a spot coverage at maximum brightness of 50 ± 15 per cent for V410 Tau, we derive an absolute unspotted magnitude of 3.17 ± 0.33 , a logarithmic luminosity $\log(L_{*}/L_{\odot}) = 0.63 \pm 0.13$, and a stellar radius $R_{*} = \sqrt{L_{*}/L_{\odot}} \times (T_{\odot}/T_{*})^2 = 3.4 \pm 0.5 R_{\odot}$. This value for the radius, combined with the $v \sin i$ derived from the spectra, yields an inclination of $53 \pm 11^{\circ}$.

The position of V410 Tau on the Hertzsprung–Russell diagram is displayed in Fig. 1. According to Siess, Dufour & Forestini (2000) stellar evolution models for PMS stars, with solar metallicity and overshooting, V410 Tau is a $1.42 \pm 0.15 M_{\odot}$ star, aged 0.84 ± 0.20 Myr and fully convective. Baraffe models (Baraffe et al. 2015) disagree with the Siess models for stars as young as V410 Tau and yield an age of < 0.5 Myr with a mass of $1.14 \pm 0.10 M_{\odot}$. However, for the sake of consistency with the other MaPP and MaTYSSE studies, we will consider the values yielded by the Siess models in this paper. Our values are in good agreement with Welty & Ramsey (1995) and Skelly et al. (2010), who had previously derived masses of ~ 1.5 and $1.4 \pm 0.2 M_{\odot}$,

¹Line-of-sight-projected equatorial rotation velocity.

²Angle between the stellar rotation axis and the line of sight.

Table 1. Physical parameters of wTTS V410 Tau. From top to bottom: distance from Earth, effective temperature, rotation period, luminosity, minimum stellar radius, stellar radius, line-of-sight-projected equatorial velocity, inclination, mass, and age.

Parameter	Value	Reference
d	129.0 ± 0.5 pc	Galli et al. (2018)
T_{eff}	4500 ± 100 K	
P_{rot}	1.87197 ± 0.00010 d	Stelzer et al. (2003)
$\log(L_*/L_\odot)$	0.63 ± 0.13	
$R_*, \sin i$	$2.708 \pm 0.007 R_\odot$	
R_*	$3.4 \pm 0.5 R_\odot$	
$v \sin i$	$73.2 \pm 0.2 \text{ km s}^{-1}$	ZDI (Section 4)
i	$50 \pm 10^\circ$	ZDI (Section 4)
M_*	$1.42 \pm 0.15 M_\odot$	
Age	0.84 ± 0.20 Myr	

respectively, radii of ~ 2.64 and $\sim 3.0 R_\odot$, respectively, and ages of 1–2 and 1.2 ± 0.3 Myr, respectively. Moreover, Skelly et al. (2010) had deduced that V410 Tau could have a radiative core of radius between $0.0 R_*$ and $0.28 R_*$. Table 1 sums up the stellar parameters of V410 Tau found in this study.

4 STELLAR TOMOGRAPHY

To map the surface brightness and magnetic topology of V410 Tau, we use the tomographic technique ZDI (Donati & Brown 1997), which inverts simultaneous time series of Stokes I and Stokes V LSD profiles into brightness and magnetic field surface maps. At each observation date, Stokes I and Stokes V profiles are synthesized from model maps by integrating the spectral contribution of each map cell over the visible half of the stellar surface, Doppler shifted according to the local RV (i.e. line-of-sight-projected velocity) and weighted according to the local brightness, cell sky-projected area, and limb darkening. The main modifier of local RV at the surface of the star is, in ZDI, the assumed rotation profile at the stellar surface, e.g. the solid-body rotation of the star or a square-cosine-type latitudinal differential rotation. Local Stokes I and Stokes V line profiles are computed from the Unno–Rachkovsky analytical solution to the polarized radiative transfer equations in a Milne–Eddington model atmosphere (this is where the local magnetic field and the Zeeman effect intervene, see Landi degl’Innocenti & Landolfi 2004). To fit the LSD profiles of V410 Tau in this study, we chose a spectral line of mean wavelength, Doppler width, Landé factor, and EW of respective values 640 nm, 1.8, 1.2, and 3.8 km s^{-1} .

Table 2. Characteristics of the ZDI models for V410 Tau at each observation epoch. *Column 1*: observation epoch. *Column 2*: number of spectropolarimetric observations used for ZDI. *Column 3*: contribution of cool (‘spots’) and hot (‘plages’) areas on the brightness map. *Column 4*: average magnetic strength, defined as the square root of the average squared magnetic field over the surface of the star. *Columns 5–7*: normalized contribution of the poloidal field, part of the poloidal field that is dipolar, and part of the poloidal field that is symmetric. *Columns 8–9*: part of the toroidal field that is dipolar and part of the toroidal field that is symmetric. *Column 10*: dipole characteristics: field strength, tilt with respect to the rotation axis, and phase of the pole. *Column 11*: systemic RV of the star as measured with ZDI, the error bar on those values is 0.20 km s^{-1} . Error bars on the magnetic field ratios are typically of 0.1.

Date	N_{obs}	Spot + plage coverage (per cent)	B (G)	r_{pol}	$r_{\text{dip/pol}}$	$r_{\text{sym/pol}}$	$r_{\text{dip/tor}}$	$r_{\text{sym/tor}}$	Dipole strength (G), tilt, and phase	RV _{bulk} (km s ⁻¹)
2008 Dec	6	5.8 + 4.4	486	0.32	0.13	0.37	0.89	0.96	129, 23°, and 0.71	16.30
2009 Jan	48	9.6 + 7.1	556	0.55	0.26	0.09	0.54	0.79	165, 54°, and 0.54	16.30
2011 Jan	20	8.1 + 6.6	560	0.40	0.24	0.23	0.72	0.85	239, 44°, and 0.62	16.40
2013 Dec	25	11.0 + 7.5	568	0.49	0.23	0.34	0.66	0.81	254, 18°, and 0.56	16.50
2015 Dec	21	8.9 + 6.7	600	0.68	0.37	0.45	0.62	0.78	458, 30°, and 0.54	16.65
2016 Jan	9	7.9 + 6.5	480	0.77	0.38	0.30	0.68	0.87	400, 44°, and 0.51	16.65

ZDI uses a conjugate gradient algorithm to iteratively reconstruct maps whose synthetic profiles can fit the LSD profiles down to a user-provided reduced chi-square (χ_r^2) level. To lift degeneracy among the multiple solutions compatible with the data at the given reduced chi square, ZDI looks for the maximal-entropy solution, considering that the minimized information from the resulting maps is the most reliable. While the brightness value can vary freely from cell to cell, the surface magnetic field is modelled as a combination of poloidal and toroidal fields, both represented as weighted sums of spherical harmonics and projected on to the spherical coordinate space (Donati et al. 2006, for the equations). In this study, the magnetic field was fitted with spherical harmonics of orders $l = 1$ to $l = 15$.

Because ZDI does not reconstruct intrinsic temporal variability except for differential rotation, there is a limit to the duration a fittable data set can span. At the same time, ZDI needs a good phase coverage from the data to build a complete map. For those reasons, ZDI was not applied to runs 2008 October and 2013 November; moreover, we reconstructed a different set of brightness and magnetic images for each of the runs on which ZDI was applied.

Using ZDI on our data yielded values for $v \sin i$ and i of 73.2 ± 0.5 and $50 \pm 10^\circ \text{ km s}^{-1}$, respectively. We also adjusted the systemic RV of V410 Tau with ZDI, and noticed a drift in the optimal value with time (see Table 2).

4.1 Brightness and magnetic imaging

Time series of Stokes I and Stokes V LSD profiles are shown in Fig. 2, both before and after removal of lunar pollution, as well as synthetic profiles generated from the reconstructed ZDI maps. The corresponding maps are shown in Fig. 3, with brightness maps in the first column and radial, meridional, and azimuthal components of the surface magnetic field in the second to fourth columns. Properties of these reconstructed maps are listed in Table 2. Since the 2008 December data set has a phase coverage of only half the star, the derived parameters characterizing the global field topology at this epoch are no more than weakly meaningful and were not used for the following analysis and discussion. Our data have been fitted down to $\chi_r^2 = 1$ with a feature coverage between 15 per cent and 18 per cent depending on the epochs, and a large-scale field strength of 0.5–0.6 kG. Since ZDI is only sensitive to mid-to large-scale surface features, and returns the maximum-entropy solution, this amount of spot coverage is not discrepant with the assumption made in Section 3; it further suggests that 30 per cent of the star is more or less evenly covered with small-scale dark features.

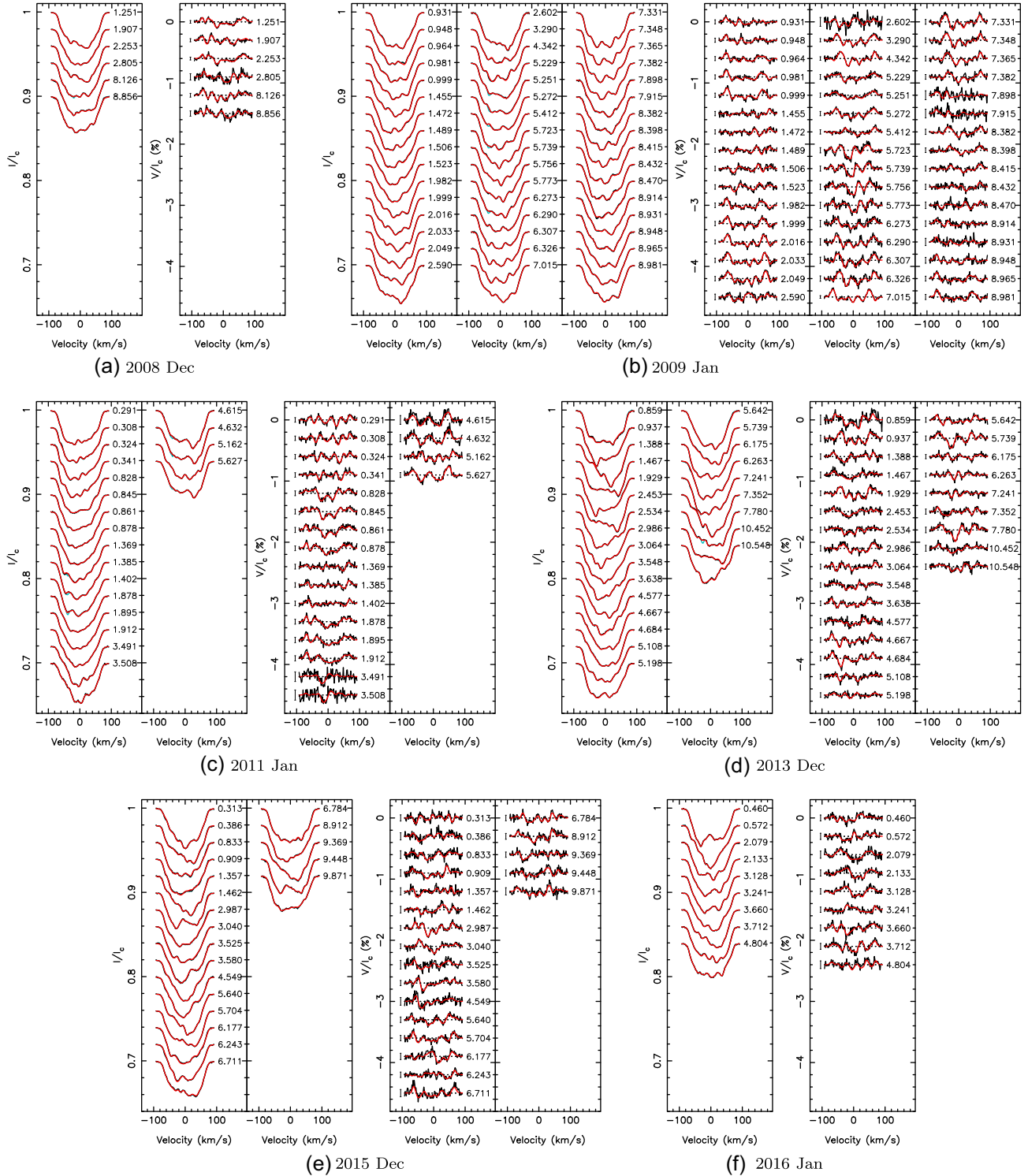


Figure 2. LSD profiles for observation epochs (a) 2008 Dec, (b) 2009 Jan, (c) 2011 Jan, (d) 2013 Dec, (e) 2015 Dec, and (f) 2016 Jan. On the right of each profile is written the corresponding rotation cycle as indicated in Table A1. The cyan, black, and red lines represent, respectively, the profiles before removal of Moon pollution, after removal of Moon pollution, and the fit obtained with Zeeman-Doppler Imaging. For each epoch, Stokes I profiles are on the left and Stokes V profiles on the right. 3σ -error bars are displayed beside each Stokes V profile.

Brightness maps display a complex structure with many relatively small-scale features, and a high contrast. At all epochs, a large concentration of dark spots is observed at the pole. In 2009 January, 2013 December, and 2015 December, the brightness map

exhibits a strong equatorial spot, respectively at phases 0.27, 0.48, and 0.48. The presence of a strong polar spot is consistent with the maps published in Skelly et al. (2010), Rice et al. (2011), and Carroll et al. (2012) for data set 2009 January. At that

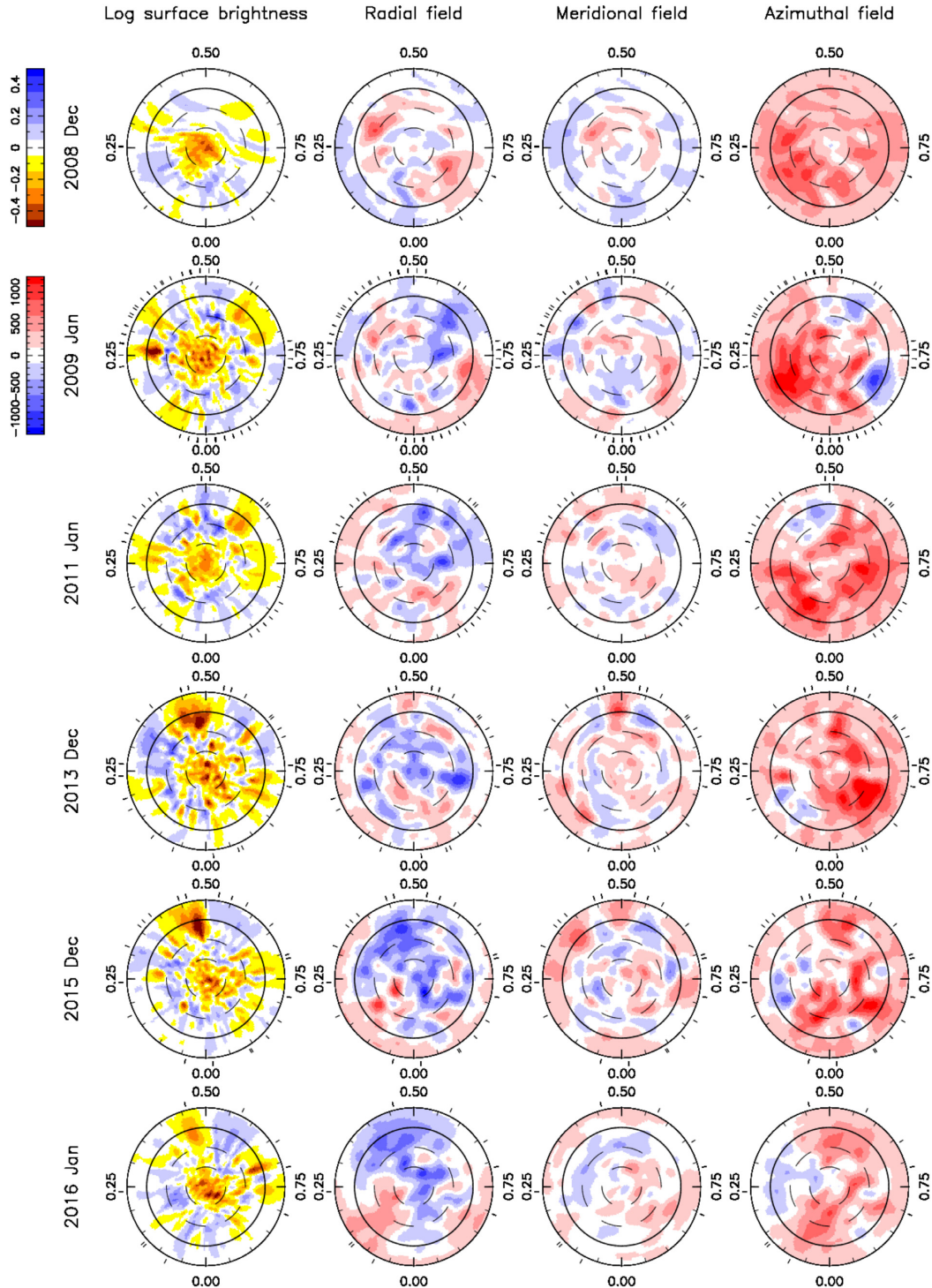


Figure 3. ZDI maps of the logarithmic relative surface brightness (first column), and the radial, meridional, and azimuthal magnetic field (second to fourth columns) of V410 Tau, reconstructed from data collected in 2008 Dec, 2009 Jan, 2011 Jan, 2013 Dec, 2015 Dec, and 2016 Jan (top to bottom rows). Each map is shown as a flattened polar view, with the equator being represented as a full line, and 60° , 30° , and -30° latitude parallels as dashed lines, and ticks around the star mark the spectropolarimetric observations. For the brightness maps, cool spots are coloured in brown and bright plagues in blue. For the magnetic maps, red represents outwards and anticlockwise field on the radial and azimuthal field maps, respectively, and the direction of the visible pole on the meridional field maps.

particular epoch, the equatorial spot at phase 0.27, and another equatorial spot at phase 0.60, are also visible in both Skelly et al. (2010) and Rice et al. (2011, fig. 8), albeit less contrasted compared to other features than they are on our map. A remnant

of the 2015 December equatorial spot is observed on the 2016 January map, where its intensity seems to have decreased, but this has to be taken with caution since ZDI maps are somewhat dependent on phase coverage. Dark spots and bright plagues

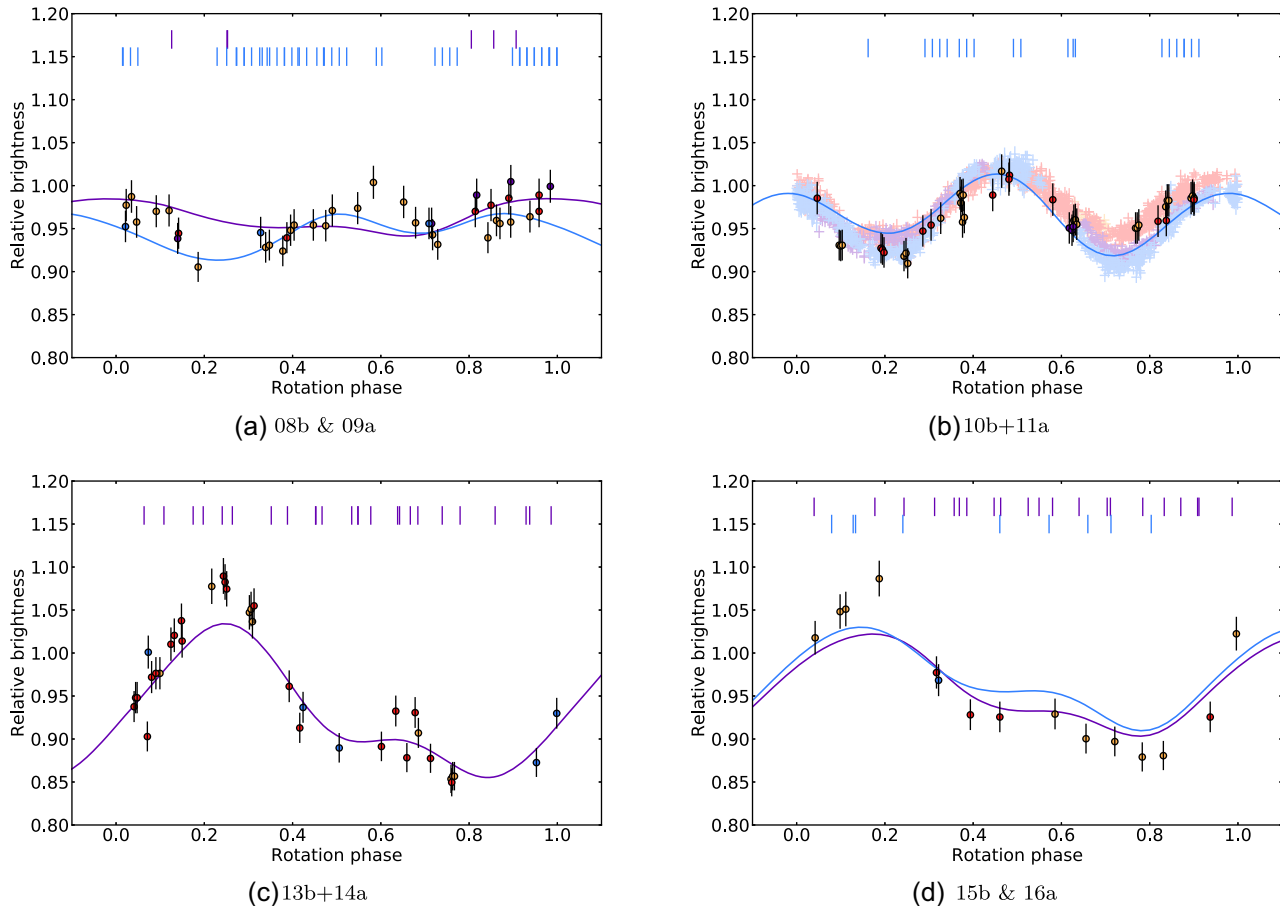


Figure 4. Phase-folded photometry data (dots with 1σ error bars) and ZDI models (lines) for observation epochs (a) 08b and 09a, (b) 10b+11a, (c) 13b + 14a, and (d) 15b and 16a. In the case of 08b and 09a and 15b and 16a, two ZDI curves are plotted for the two ZDI maps reconstructed within each epoch. Orange, red, purple, and blue colours each indicate a quarter of the total time span of the observations (photometric and spectropolarimetric together), in chronological order. Spectropolarimetric observations are marked by ticks above the light curves. In panel b, WASP data were added as desaturated crosses, with the size of the cross branches indicating their 1σ error bars.

contribute to the feature coverage at about 9 percent/7 percent, respectively.

Photometry curves from the ZDI brightness maps were synthesized and a comparison to contemporary CrAO data, and WASP data in the case of 2011 January, is shown in Fig. 4. Despite a slightly underestimated amplitude at phase 0.60 in 2008b–2009a, at phase 0.20 in 2011a, at phase 0.20 in 2013b, and at phases 0.20 and 0.80 in 2015b–2016a, ZDI manages to retrieve the measured photometric variations of V410 Tau rather satisfyingly. We notice a small temporal evolution of the light curve in the WASP data during season 2010b–2011a, where the regions around phases 0.20 and 0.70 globally darken by 0.02–0.03 mag ($\simeq 4\sigma$) over the 4 months that the data set spans.

The magnetic field maps also show a high complexity, with a poloidal component that has a weak dipolar contribution and that is rather non-axisymmetric, and a toroidal component contributing to ~ 50 per cent of the overall magnetic energy in 2009, 2011, and 2013, and decreasing towards $\simeq 30$ per cent in 2015–2016, that is both strongly dipolar and highly axisymmetric. The dipole pole is tilted at various angles depending on the epoch, with a tilt as high as 54° in 2009 January, down to 18° in 2013 December. The phase of the pole is always around 0.50–0.60, and the intensity of the poloidal dipole increases over time, from 165 G in 2009 January

to $\simeq 400$ G in 2015–2016. We note that the maximum emission of H α corresponds to the phase at which the dipole is tilted (Fig. C1). For visualization purposes, three-dimensional potential fields were extrapolated from the radial components of the magnetic maps, and displayed in Fig. 5, with phase 0.50 facing the reader.

We do not observe a particular correlation between our brightness and our magnetic maps, meaning the areas with strong magnetic field are not necessarily crowded with dark spots, according to the ZDI reconstruction.

4.2 Differential rotation

Without differential rotation, ZDI cannot fit an extended data set, such as 2008 December + 2009 January, 2013 November + 2013 December, or 2015 December + 2016 January (shortened in this subsection to 08b + 09a, 13b, and 15b + 16a, respectively), down to $\chi_r^2 = 1$, it only manages to reach values of 1.66, 1.20, and 2.64, respectively. This implies that some level of variability exists and impacts the data on time-scales of a few months, which could come from the presence of differential rotation at the surface of V410 Tau. We model differential rotation with the following law:

$$\Omega(\theta) = \Omega_{\text{eq}} - (\cos \theta)^2 d\Omega,$$

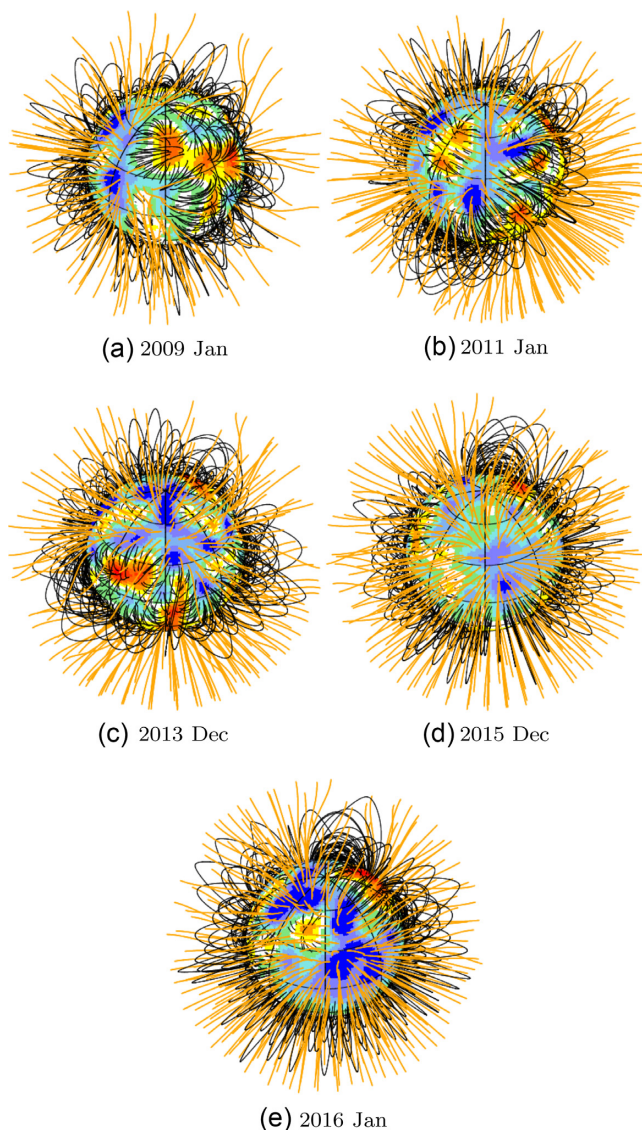


Figure 5. Potential field extrapolations of the ZDI-reconstructed surface radial field, as seen by an Earth-based observer, for observation epochs (a) 2009 Jan, (b) 2011 Jan, (c) 2013 Dec, (d) 2015 Dec, and (e) 2016 Jan at phase 0.50. Open/closed field lines are shown in orange/black, respectively, and colours on the stellar surface depict the local value of the radial field (in G, as shown in the left-hand panels of Fig. 3). The source surface at which field lines open is set to $2.1 R_*$, corresponding to the corotation radius and beyond which field lines are expected to quickly open under centrifugal forces given the high rotation rate of V410 Tau.

where θ is the colatitude, Ω_{eq} the equatorial rotation rate, and $d\Omega$ the pole-to-equator rotation rate difference. We constrain Ω_{eq} and $d\Omega$ by pre-setting the amount of information ZDI is allowed to reconstruct, and having ZDI minimize the χ_r^2 in these conditions.

We performed this analysis on the three aforementioned extended data sets, and on Stokes I and Stokes V time series separately, reconstructing only brightness or only magnetic field, respectively. From the resulting χ_r^2 maps over the $\{\Omega_{\text{eq}}, d\Omega\}$ space, one can plot the contours of the 1σ (68.3 per cent) and 3σ (99.7 per cent) areas of confidence for each observation epoch. Fig. 6, which shows such contours, highlights clear minima surrounded by almost elliptic areas of confidence at each epoch, and shows that each 3σ -confidence area overlaps at least two other 3σ -

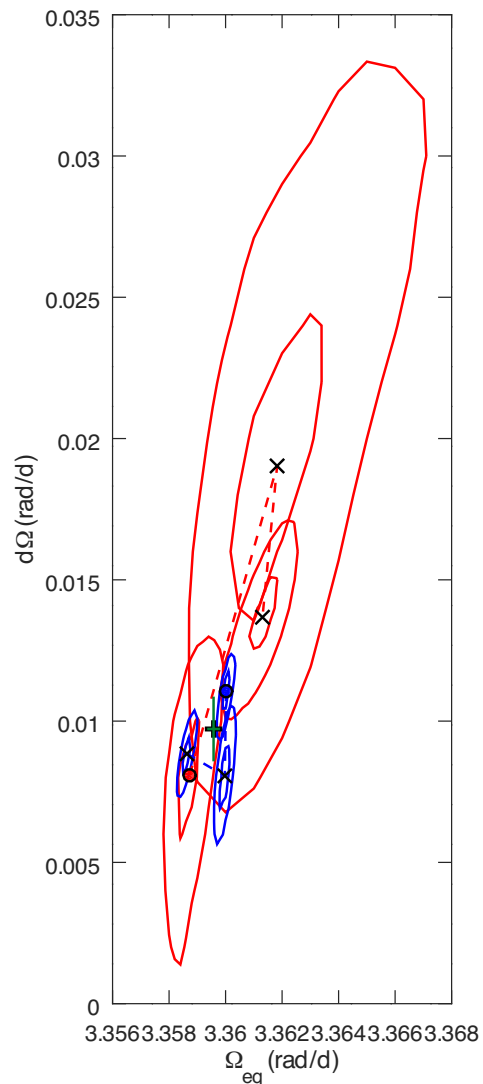


Figure 6. Evolution of the differential rotation of V410 Tau as measured from Stokes I (blue) and Stokes V (red) profiles. The points corresponding to observation epoch 2008b–2009a are marked with o symbols, then the dashed lines link the epochs in chronological order (2013b–2014a and 2015b–2016a are marked with x symbols). 68.3 per cent and 99.7 per cent contours of confidence are displayed for each observation epoch. The weighted average of the six measurements, chosen to produce the maps shown in Section 4, is represented as a black $+$, with overlaid error bars in green.

confidence areas. Numerical results for each epoch are given in Table 3. We chose to use a unique set of parameters to reconstruct all images shown in Section 4: the weighted means of the six seasonal minima, $\Omega_{\text{eq}} = 3.35957 \pm 0.00006 \text{ rad d}^{-1}$ and $d\Omega = 0.0097 \pm 0.0003 \text{ rad d}^{-1}$.

Following the method described in Donati, Collier Cameron & Petit (2003), we computed, for each epoch, the colatitude at which the rotation rate is constant along the confidence ellipse major axis. This value corresponds to the colatitude where the barycentre of the brightness/magnetic features imposing a correlation between Ω_{eq} and $d\Omega$ are located. For both Stokes I and Stokes V , we note a slight increase with time of the cosine of this colatitude (Table 3), i.e. an increase in the barycentric latitude of the dominant features of $5 \pm 2^\circ$ and $15 \pm 5^\circ$, respectively.

Table 3. Summary of differential rotation parameters obtained for V410 Tau on each season. All rotation rates are given in mrad d^{-1} . Column 2 gives the total number of data points used in the imaging process, then columns 3–7 correspond to Stokes I data while column 8–12 correspond to Stokes V data. Columns 3 and 8 list the derived equatorial rotation rate Ω_{eq} , with its 68 per cent (i.e. 1σ) confidence interval, columns 4 and 9 the difference in rotation rate $d\Omega$ between the equator and pole, with its 68 per cent confidence interval, columns 5 and 10 give the reduced chi square of the ZDI model compared to the data, columns 6 and 11 give the inverse slope of the ellipsoid in the $\Omega_{\text{eq}}-d\Omega$ plane (also equal to $\cos^2 \theta_s$, where θ_s denotes the colatitude of the gravity centre of the spot distribution, see Donati et al. 2000), and columns 7 and 12 give the rotation rate Ω_s at colatitude θ_s .

Epoch	n	Stokes I data / brightness reconstruction					Stokes V data / magnetic field reconstruction				
		Ω_{eq}	$d\Omega$	χ_r^2	$\cos^2 \theta_s$	Ω_s	Ω_{eq}	$d\Omega$	χ_r^2	$\cos^2 \theta_s$	Ω_s
08b + 09a	5562	3360.0 ± 0.1	11.1 ± 0.6	1.276	0.12 ± 0.03	3358.7 ± 0.4	3358.7 ± 0.3	8.1 ± 1.8	1.127	0.11 ± 0.03	3357.9 ± 0.5
13b	2781	3360.0 ± 0.1	8.1 ± 0.7	1.341	0.11 ± 0.03	3359.1 ± 0.3	3361.8 ± 1.3	19.0 ± 4.3	1.038	0.23 ± 0.03	3354.6 ± 2.1
15b + 16a	3090	3358.6 ± 0.1	8.8 ± 0.5	2.583	0.18 ± 0.03	3357.0 ± 0.4	3361.3 ± 0.4	13.7 ± 1.0	1.046	0.32 ± 0.03	3352.7 ± 0.8

These models exclude solid-body rotation at a level of 3.6σ to 22σ depending on the epoch. We note that, even with differential rotation, ZDI cannot fit the data of 08b + 09a and of 15b + 16a down to $\chi_r^2 = 1$, no matter the amount of information allowed. This indicates that surface features are also altered by a significant level of intrinsic variability within the 2 month span of our data set. This issue is further discussed in section 5.3.

5 RADIAL VELOCITIES

Radial velocity values were derived as the first-order moment of the continuum-subtracted Stokes I LSD profiles, for all spectra except the three with low S/N and the six in which we identified flares (see Table A1). The raw RVs we obtain contain a contribution from the inhomogeneities on the photosphere, called activity jitter, which we aim to filter out in order to access the actual RV of the star, and look for a potential planet signature. The activity jitter is modelled with two different techniques, ZDI and GPR. Raw RVs and jitter models are plotted in Fig. 7 and listed in Table A1. For the 2015–2016 points, a new version of ZDI, with the logarithmic brightness of surface features allowed to linearly vary with time, was tested (section 5.3). The raw RVs present modulations whose amplitude vary between 4 and 8.5 km s^{-1} , with a global rms of 1.8 km s^{-1} . Like with the photometric data, the RV variations are the lowest in 2009 January and the strongest in 2013 December.

5.1 Activity jitter

The first method consists in deriving the activity jitter from the ZDI models (see Fig. 2), computed as the first-order moment of the continuum-subtracted synthetic Stokes I profiles. Indeed, when computing the raw RV from the observed Stokes I LSD profiles, this activity jitter is added on top of the radial motion of the star as a whole. We model the activity jitter separately for epochs 2009 January, 2011 January, 2013 December, 2015 December, and 2016 January (excluding 2008 December because of the poor phase coverage).

The second method uses GPR (Haywood et al. 2014; Donati et al. 2017), a numerical method focusing on the statistical properties of the model. In short, GPR extrapolates a continuous curve described by a given covariance function from some given data points. To describe the activity jitter here, we use a pseudo-periodic covariance function:

$$K(t, t') = \theta_1^2 \exp \left[-\frac{(t - t')^2}{\theta_3^2} - \frac{\sin^2 \left(\frac{\pi(t - t')}{\theta_2} \right)}{\theta_4^2} \right], \quad (2)$$

where t and t' are the dates of the two RV points between which the covariance is computed, θ_1 is the amplitude of the GP, θ_2

the recurrence time-scale (expected to be close to P_{rot}), θ_3 the decay time-scale (i.e. the typical spot lifetime in the present case), and θ_4 a smoothing parameter (within $[0, 1]$) setting the amount of high-frequency structures that we allow the fit to include. The modelling process therefore consists in optimizing the four parameters θ_1 , θ_2 , θ_3 , and θ_4 , called hyperparameters. To do so, we use a Markov Chain Monte Carlo algorithm, and allocate to each point of the hyperparameter space a likelihood value, which takes into account both the quality of the fit and some penalizations on the hyperparameters (for example we penalize high amplitudes, low decay times, and low smoothings). The priors are listed in Table 4. The phase plot of the MCMC is displayed in Fig. 8 and the best fit is shown in Fig. 7, together with the ZDI fits. We note that, contrary to ZDI, GPR, being capable of describing intrinsic variability in a consistent way, is able to fit our whole 8 yr long data set with one model. We obtain $\theta_1 = 1.8_{-0.2}^{+0.2} \text{ km s}^{-1}$, $\theta_2 = 0.9991 \pm 0.0002 P_{\text{rot}}$, $\theta_3 = 86_{-19}^{+24} P_{\text{rot}}$, and $\theta_4 = 0.35 \pm 0.03 P_{\text{rot}}$.

The rms of the filtered RVs for each epoch and each method are summarized in Table 5. The RV curve filtered from the ZDI model presents a global rms of 0.167 km s^{-1} , i.e. $\sim 2 < \sigma_{\text{RV}} >$ (see Table A1). The epoch where the filtering is most efficient is 2009 January, although the rms of the filtered RVs is only at $1.5 < \sigma_{\text{RV}} >$, and it goes up to $3 < \sigma_{\text{RV}} >$ in 2011 January and 2013 December. On the other hand, the GPR model filters the RV out down to $0.076 \text{ km s}^{-1} = 0.94 < \sigma_{\text{RV}} >$.

5.2 Periodograms

Lomb–Scargle periodograms for both raw and filtered RVs, for both methods (Fig. 9 for each individual epoch, Fig. 10 for the whole data set), show that the stellar rotation period or its first harmonic are clearly present in 2009 January and 2011 January, but not well retrieved in 2013 December, 2015 December, and 2016 January. However the periodogram for the whole RV_{raw} data set presents neat peaks at P_{rot} and its first two harmonics. P_{rot} and its first harmonic are well filtered out by both modelling methods, and the second harmonic is well filtered out in the GP residuals. A weak signal remains at $P_{\text{rot}}/3$ in the ZDI residuals but looking at a phase-folded plot does not reveal any particularly obvious tendency, leading us to suspect that it mostly reflects the contribution of a few stray points. No other period stands out with a false-alarm probability lower than 5 per cent, which allows us to conclude that no planet signature is found in this data set with our filtering methods.

5.3 New ZDI: with short-time intrinsic evolution

Seeing that the filtered RVs when using GPR have an rms twice lower than when using ZDI (Table 5), we try to improve our ZDI filtering process by implementing a new feature: instead of only

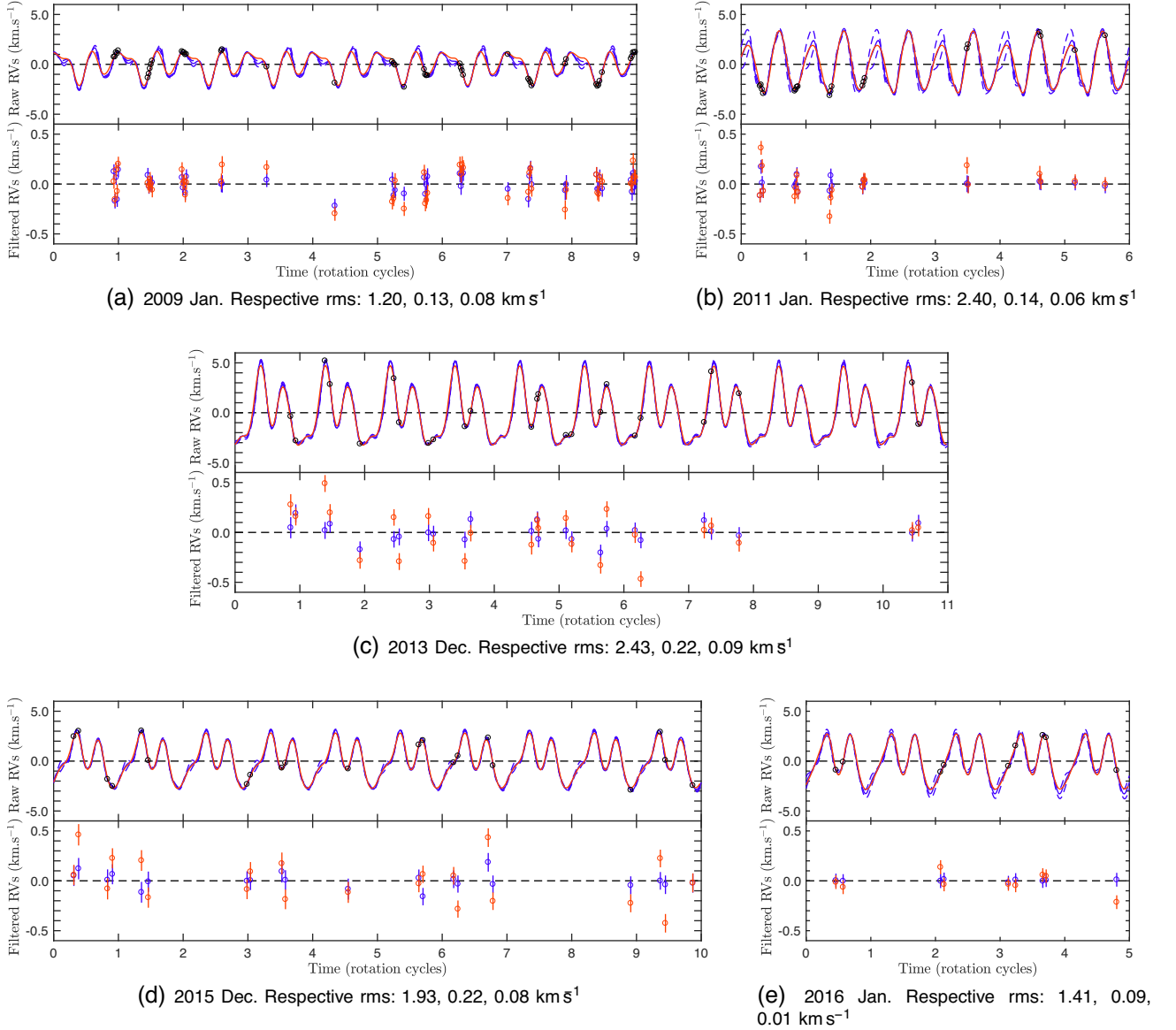


Figure 7. Raw and filtered RVs of V410 Tau for each observation epoch. On each figure, the top plot depicts the raw RVs (red dots), the ZDI reconstruction (red full line), and the GP fit (blue full line with 1σ area of confidence marked as blue dashed lines, see Section 5.1). The bottom plot depicts the RVs filtered from the ZDI-modelled activity (red dots) and the RVs filtered from the GP-modelled activity (blue dots). The subcaptions indicate the rms of the raw RVs, the ZDI-filtered RVs, and the GPR-filtered RVs, respectively. All rotational cycles are displayed as in Table A1.

Table 4. Priors for our GP-MCMC run on our raw RVs. For the modified Jeffreys prior, the knee value is given, for the Gaussian prior we give the mean and standard deviation, and for the Jeffreys and the uniform priors we give the lower and upper boundaries.

Hyperparameter	Prior
θ_1 (km s ⁻¹)	Modified Jeffreys (σ_{RV})
θ_2 (P_{rot})	Gaussian (1.0000, 0.1000)
θ_3 (P_{rot})	Jeffreys(0.1, 500.0)
θ_4	Uniform (0, 1)

having one brightness value in each cell, we give it a brightness value and an evolution parameter, so that ZDI brightness maps are allowed to evolve with time to better fit time series of LSD profiles with variability. Thus we reconstruct two maps for the brightness:

the brightness at time 0 and the map of the evolution parameter. We choose, for now, a simple model where the logarithmic relative brightness of each cell k is allowed to evolve linearly with time:

$$\log Q_k(t) = \log Q_k(0) + m_k t, \quad (3)$$

where $Q_k(t)$ is the local surface brightness and m_k is the evolution parameter. Applying this new method to the 2015–2016 extended data set, we manage to fit the whole data set down to a χ_r^2 of 1 where classical ZDI, even with differential rotation, could not reach lower than $\chi_r^2 = 2.5$ (see Section 4.2). Maps associated with this reconstruction are shown in Fig. 11, and derived RVs are plotted in Figs 12 and 13, to be compared with RVs derived from classical ZDI maps. The rms of the filtered RVs here, 0.194 km s⁻¹, does not decrease compared to when using classical ZDI, which means our model is still too simple and cannot fully account for the observed

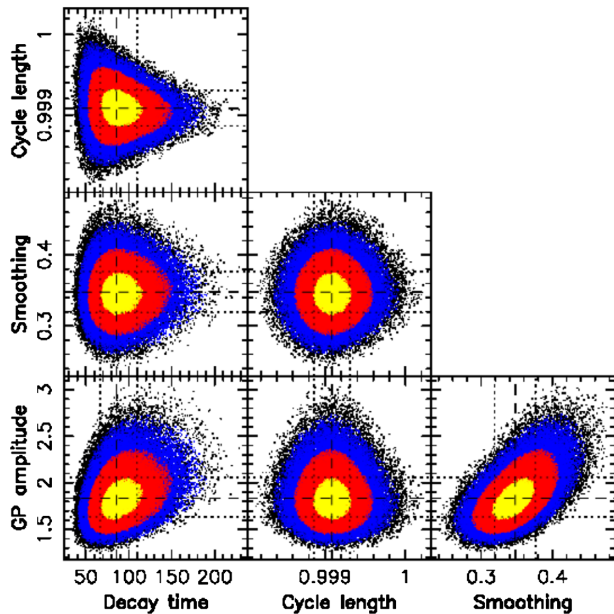


Figure 8. Phase plot of the MCMC–GPR run on the raw RVs, model without planet. The yellow, red, and blue colours indicate respectively the 1σ , 2σ , and 3σ areas of confidence, and the optimal values for the hyperparameters are marked with black dashed lines, with 1σ intervals marked with black dotted lines. GP amplitude (θ_1): $1.8^{+0.2}_{-0.2}$ km s $^{-1}$, Cycle length (θ_2): $0.9991 \pm 0.0002 P_{\text{rot}}$, Decay time (θ_3): $86^{+24}_{-19} P_{\text{rot}}$, Smoothing (θ_4): 0.35 ± 0.03 .

Table 5. Rms of RVs. All rms RVs are given in km s $^{-1}$.

Epoch	2009	2011	2013	2015	2016	All
Raw	1.200	2.392	2.429	1.932	1.411	1.8
ZDI filt.	0.131	0.141	0.215	0.222	0.094	0.167
GP filt.	0.084	0.064	0.087	0.075	0.009	0.076

variability. However, Fig. 13 shows that global trends in the temporal evolution of the RV curve are well reproduced by this new ZDI model, such as the jitter maximum moving from phase 0.37 to 0.32, or the local minimum at phase 0.54 in 2015 December moving to 0.50 in 2016 January.

6 SUMMARY AND DISCUSSION

This paper reports the analysis of an extended spectropolarimetric data set on the ~ 0.8 Myr wTTS V410 Tau, taken with the instruments ESPaDOnS at CFHT and NARVAL at TBL, spanning 8 yr and split between six observation epochs (2008b, 2009a, 2011a, 2013b, 2015b, and 2016a), the last three of which were observed as part of the MaTYSSSE observation programme. Contemporaneous photometric observations from the CrAO and from the WASP programme complemented the study. ESPaDOnS, NARVAL, and CrAO observations are documented in Appendix A (available online).

V410 Tau is composed of an inner close binary (V410 Tau A-B) around which orbits a third component (C Ghez et al. 1997), with V410 Tau A being much brighter than the other two in the optical domain, and thus the star that our data inform. The stellar parameters derived in this work are summed up in Table 1: at ~ 0.8 Myr, V410 Tau is a $1.42 \pm 0.15 M_{\odot}$ and $3.4 \pm 0.5 R_{\odot}$ wTTS.

6.1 Activity and magnetic field of V410 Tau

Applying LSD then ZDI on our data set, we estimated the $v \sin i$ and inclination of V410 Tau at 73.2 ± 0.5 and $50 \pm 10^{\circ}$ km s $^{-1}$, respectively. Considering the well-determined rotation period of 1.871970 ± 0.000010 (Stelzer et al. 2003) and the minimal observed visible magnitude of 10.52 (Grankin et al. 2008), this implies a relatively high level (~ 50 per cent) of spot coverage. We reconstructed brightness and magnetic surface maps at each observation epoch, constrained the differential rotation, and found a drift in the bulk radial velocity. Our ZDI brightness maps display a relatively highly spotted surface: the spot coverage reaches 6.5–11.5 per cent depending on the epoch (not counting 2008 December where only half the star was imaged) and the plage coverage is found around 7 per cent at all epochs. Since ZDI mostly recovers large non-axisymmetric features and misses small ones evenly distributed over the star, the spot and plage coverage is underestimated, which makes this result compatible with the spot coverage obtained from the aforementioned V magnitude measurements. We note that V410 Tau being heavily spotted makes it difficult to pinpoint its age. We fit a two-temperature model (photosphere at 4500 K and fixed-temperature spots with a varying filling factor) into our $B - V$ and V magnitude data, and found an optimal spot temperature of around 3750 K, which implies a contrast of ~ 750 K between dark spots and the photosphere (see Fig. B7). This contrast is slightly lower than the one retrieved for the 2 Myr wTTS LkCa 4 in Gully-Santiago et al. (2017). V410 Tau always presents a high concentration of dark spots around the pole, and several big patches of dark spots on the equator.

V410 Tau has a relatively strong large-scale magnetic field, with an average surface intensity that is roughly constant over the years at 550 ± 50 G. Its radial field reaches local values beyond -1 and $+1$ kG in several epochs. The brightness and magnetic surface maps both present some variability from epoch to epoch (Fig. 3, Table 2), which points to a dynamo-generated magnetic field rather than a fossil one. The magnetic energy is, at all epochs, equally distributed between the poloidal and toroidal components of the field, with the poloidal component being rather non-dipolar and non-axisymmetric, whereas the toroidal component is mostly dipolar and axisymmetric. The poloidal dipole, tilted towards a phase that stays within 0.6 ± 0.1 during the whole survey, but at an angle varying between 20° and 55° depending on the epoch, sees its intensity increase almost monotonously from 165 to 458 G over 8 yr, and the dipolar contribution to the poloidal field also increases from ~ 25 per cent to ~ 40 per cent (see Table 2).

The toroidal component, which displays a constant orientation throughout our data set, is unusually strong compared to other fully convective rapidly rotating stars (e.g. V830 Tau is 90 per cent poloidal, see Donati et al. 2017). A similarly strong toroidal field was observed on one other MaTYSSSE target, LkCa 4 (Donati et al. 2014). The origin of this strong toroidal field is still unclear: could it be maintained by an α^2 dynamo, like in the simulations of low-Rossby fully convective stars by Yadav et al. (2015)? The remnants of a subsurface radial shear between internal layers accelerating due to contraction, and disc-braked outer layers? Or would the even earlier toroidal energy, from right after the collapse of the second Larson core (as found in the simulations of Vaytet et al. 2018), somehow not have entirely subsided yet? Would the early dissipation of the disc, a common factor between LkCa 4 and V410 Tau, have something to do with this?

At ~ 0.8 Myr, V410 Tau is one of the youngest observed wTTSs (Kraus et al. 2012; Fig. 3). Assuming that, when the disc was present,

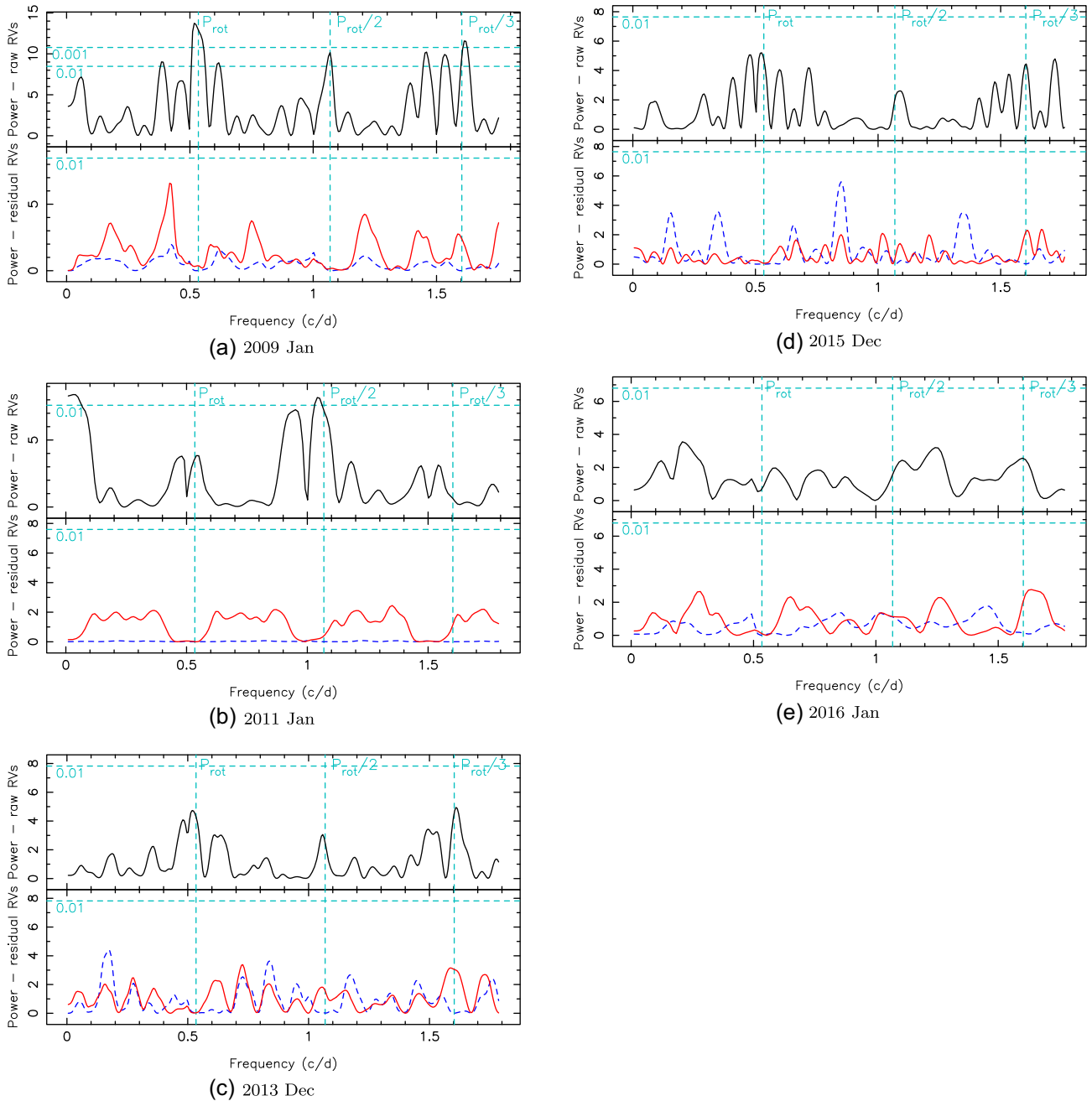


Figure 9. Periodograms of the raw RVs (top), of the ZDI-filtered RVs (bottom, red full line) and of the GP-filtered RVs (bottom, blue dashed line), for observation epochs (a) 2009 Jan, (b) 2011 Jan, (c) 2013 Dec, (d) 2015 Dec, and (e) 2016 Jan. False-alarm probability levels of 1 per cent and 0.1 per cent are represented as horizontal cyan dashed lines, and P_{rot} and its first two harmonics as vertical cyan dashed lines.

V410 Tau was magnetically locked to it at a rotation period of ~ 8 d with a cavity of ~ 0.085 au (similarly to cTTSs BP Tau, AA Tau, and GQ Lup, see Donati et al. 2008, 2010b, 2012, respectively), then V410 Tau should have had a radius of $\sim 7R_{\odot}$ when the disc dissipated, to match the angular momentum that we measure today (Bouvier 2007). According to the Siess models (Siess et al. 2000), this corresponds to an age of ~ 0.2 Myr. With a radius of $\sim 7R_{\odot}$, V410 Tau would have needed a magnetic dipole barely above 100 G to maintain the assumed magnetospheric cavity, even with an accretion rate of $\sim 10^{-8} M_{\odot} \text{ yr}^{-1}$ just before disc dissipation. That value is compatible with the 200–400 G dipole we measure on the

$\sim 3.5 R_{\odot}$ star today. Kraus et al. (2012; Fig. 1) shows a correlation between the presence of a close companion and the early depletion of the accretion disc, which indicates that V410 Tau B, observed at a projected separation of 16.8 ± 1.4 au (Ghez et al. 1995), could have been responsible for the early depletion of the disc.

In our H α dynamic spectra, we observe a conspicuous absorption feature in the second part of the 2009 January run around phase 0.95 (Fig. C1), that could be the signature of a prominence (see e.g. Collier Cameron & Woods 1992). Fitting a sine curve in the absorption feature yields an amplitude of $\sim 2 v \sin i$, corresponding to a prominence $\sim 2 R_{*}$ away from the centre of V410 Tau, confirm-

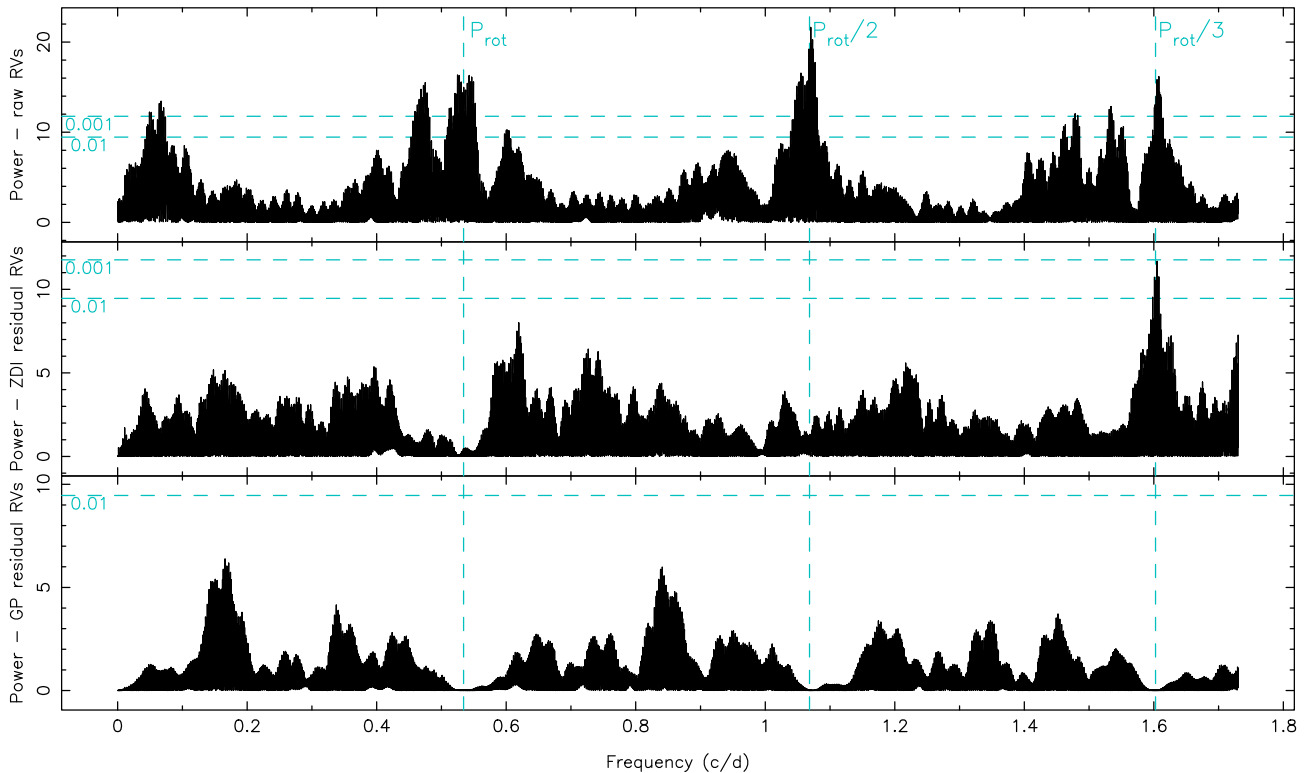


Figure 10. Periodograms of the raw RVs (top), of the RVs filtered from ZDI-modelled activity (middle) and of the RVs filtered from GP-modelled activity (bottom, blue dashed line), for observation epochs (a) 2009 Jan, (b) 2011 Jan, (c) 2013 Dec, (d) 2015 Dec, and (e) 2016 Jan. Periodograms of the whole data set raw RVs (top), RVs filtered from ZDI-modelled activity (middle) and RVs filtered from GP-modelled activity (bottom). False-alarm probability levels of 1 per cent and 0.1 per cent are represented as horizontal cyan dashed lines, and P_{rot} and its first two harmonics as vertical cyan dashed lines.

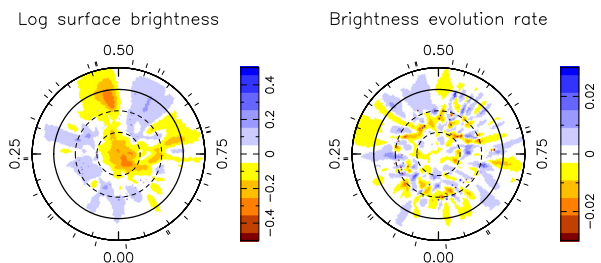


Figure 11. Brightness map and evolution rate reconstructed by ZDI on data set 2015 Dec–2016 Jan. Pole-on view with the equator being represented as a full line, and 60° , 30° , and -30° latitude parallels as dashed lines. Cool spots are coloured in brown and bright plages in blue, and ticks around the star mark the spectropolarimetric observations.

ing that the prominence is located close to the corotation radius. Plotting the 3D potential field extrapolation of the reconstructed surface radial field for 2009 January, at phases 0.95, 0.20, 0.45, and 0.70, we observe the presence of closed field lines reaching $\sim 2R_*$ at phase 0.95 (Fig. 14), which may be able to support the observed prominence. We also observe similar absorption features in 2009 January around phase 0.8 and in 2011 January around phase 0.35, but they are less well covered by our observations. We however found corresponding field lines at the right phase for each (see Fig. 14 for 2009 January).

We also constrained the differential rotation of V410 Tau with ZDI: we obtained six values for the equatorial rotation rate Ω_{eq} and for the pole-to-equator rotation rate difference $d\Omega$, by using separately our Stokes I and Stokes V LSD profiles from each of

the three data sets 2008b + 2009a, 2013b, and 2015b + 2016a. Overall mean values are $\Omega_{\text{eq}} = 3.35957 \pm 0.00022 \text{ rad d}^{-1}$ and $d\Omega = 0.0097 \pm 0.0011 \text{ rad d}^{-1}$. The differential rotation of V410 Tau is thus relatively weak, with a pole-to-equator rotation rate difference 5.6 times smaller than that of the Sun, and a lap time of $648 \pm 73 \text{ d}$. Compared to other wTTSs previously analysed within the MaTYSSSE programme, the differential rotation of V410 Tau is similar to that of V830 Tau (Donati et al. 2017) but much smaller than that of TAP 26, which is almost of solar level, consistent with the fact that TAP 26 is no longer fully convective and has developed a radiative core (of size $0.6R_*$, Yu et al. 2017).

6.2 Mid-term variability of V410 Tau

Even with differential rotation, it is impossible for our current version of ZDI to model data sets spanning a few months down to noise level, which shows that the surface of V410 Tau undergoes significant intrinsic variability, corroborating the hypothesis of a dynamo-generated field. The variations of the photosphere and of the surface magnetic field over the years might be the manifestation of a magnetic cycle, whose existence has been suggested by previous studies (Stelzer et al. 2003; Hambálek et al. 2019). No clear change in $d\Omega$ is observed while the dipole grows in intensity (Table 3), which could indicate a time lag in the dynamo interaction between the magnetic field and the rotation profile.

The bulk RV of V410 Tau exhibits a drift throughout our 8 yr campaign, from $16.30 \pm 0.05 \text{ km s}^{-1}$ in 2008b–2009a to $16.65 \pm 0.05 \text{ km s}^{-1}$ in 2015b–2016a. One explanation could be a variation in the suppression of convective blueshift in regions of

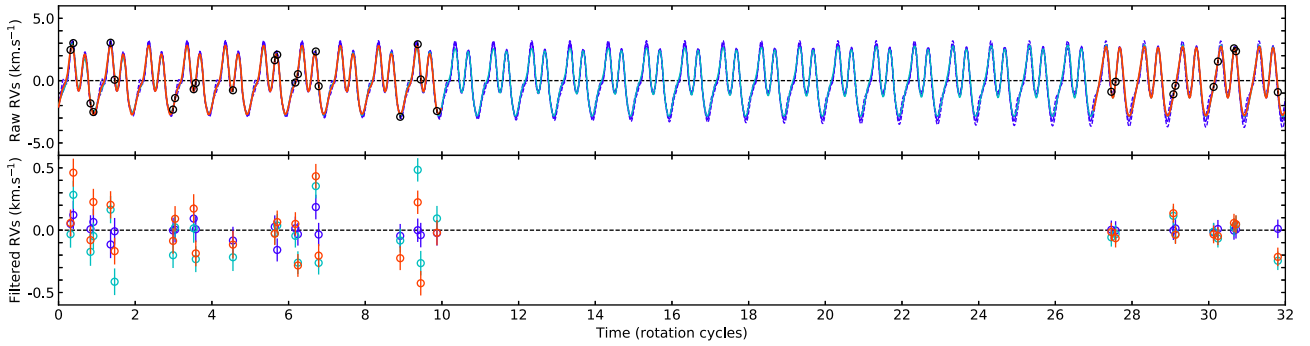


Figure 12. Comparison between the GP model, the new ZDI model, and the classical ZDI models for V410 Tau RVs in season 2015b–2016a. Rotation cycles are offset to concur with Table A1. Top: raw RVs (black dots) with 1σ error bars, GP model (purple full line), new ZDI model (cyan full line), and classical ZDI models for both observation epochs 2015 Dec and 2016 Jan (red full lines). Bottom: RVs filtered from the GP model (purple dots), from the new ZDI model (cyan dots), or from the classical ZDI models (red dots). The rms of the filtered RVs with GP, new ZDI, and classical ZDI are, respectively, 0.065, 0.194, and 0.193 km s^{-1} .

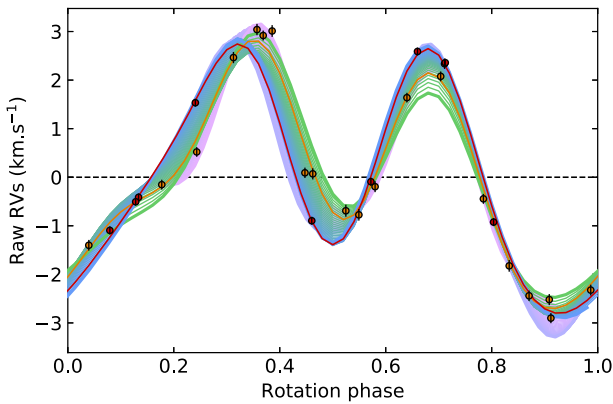


Figure 13. Raw RVs of V410 Tau in the 2015b–2016a season, between cycles 1349 and 1381 as referenced in Table A1, plotted against stellar rotation phase. The GPR and new ZDI models are represented by full lines coloured in gradients, from earliest to latest cycle, respectively, pink to purple and green to blue, while the classical ZDI models for 2015 Dec and 2016 Jan are plotted in orange and red, respectively. Observations are plotted as dots with 1σ error bars, orange for 2015 Dec and 2016 Jan.

strong magnetic field (Meunier, Desort & Lagrange 2010; Haywood et al. 2016), which could further support a secular evolution of the magnetic topology. It could also be a manifestation of the binary motion of V410 Tau A-B. The central binary of V410 Tau was observed twice, with a sky-projected separation of 16.8 ± 1.4 au in 1991 October and 9.5 ± 0.3 au in 1994 October (0.13 ± 0.01 arcsec and 0.074 ± 0.002 arcsec, respectively, in Ghez et al. 1995), and a mass ratio of 0.20 ± 0.10 (Kraus et al. 2011). Assuming a mass ratio of 0.2 and an edge-on circular orbit, we find that an orbit of the primary star of radius 6.0 au, i.e. binary separation 36.0 au and period 166 a, fits our bulk RVs and the sky-projected separations at a level of 2σ (see Fig. 15). No binary motion was detected in the 2013–2017 astrometry measurements of Galli et al. (2018), which is consistent with our model where the sky-projected velocity varies by only 0.13 mas a^{-1} over these 3.5 yr (roughly a 50th of the orbital period). More measurements would enable to estimate the eccentricity and potentially fit the sky-projected separations to a better level, as well as to decide whether the binary motion can explain the RV drift observed in this study.

The rotation period derived from our V magnitude measurements, in each observing season, also displays long-term variations. Placing the periods found from the photometric data on a period-latitude diagram representing the modelled differential rotation (Fig. B5), we observe that the latitudes corresponding to the successive periods tend to increase from 0 in 2008 to $\sim 50^\circ$ in 2016. We note that this trend is observed with both the periods derived from sine fits to the photometric data and those derived from GPR (see Appendix B, available online). This implies that the largest features, i.e. those with the biggest impact on the photometric curve, underwent a poleward migration, reminiscent of the Solar butterfly diagram (albeit reversed). This would suggest that the dynamo wave, if cyclic, has a period of at least 8 a and likely much longer (16 a if our data covers only one half of a full cycle). Previous studies using different data have suggested the existence of an activity cycle on V410 Tau, with periods of 5.4 and 15 a, respectively (Stelzer et al. 2003; Hambálek et al. 2019). We further note that our differential rotation measurements confirm that the barycentre of surface features migrates to higher latitudes over time (see Fig. 6).

Applying GPR with MCMC parameter exploration to our $H\alpha$ EWs and longitudinal magnitude field measurements (B_ℓ , first-order moment of the Stokes V LSD profiles, Donati & Brown 1997), we also found rotation periods from which we derive mean barycentric latitudes of features constraining the modelling of each quantity (see Fig. 16). The period found from $H\alpha$ is equal within error bars to the one derived in Stelzer et al. (2003) from photometry, whereas the period found from B_ℓ seems tied to equatorial features. It is worth mentioning that we also find long decay times for these two activity proxies: 589_{-335}^{+774} and 604_{-289}^{+553} d, respectively, which suggests, with the caution needed with such high error bars, that the $H\alpha$ and B_ℓ modulations are particularly sensitive to large, long-lasting features. The phase plots are displayed in Appendix C (available online).

6.3 Radial velocity modulations

We modelled the activity RV jitter from line profiles synthesized from our ZDI maps, and filtered it out from the RV curve of V410 Tau. From an rms of 1.802 km s^{-1} in the raw RVs, we get residuals with an rms of 0.167 km s^{-1} . We also applied GPR to our raw RVs and found a jitter of periodicity 1.87029 ± 0.00037 d and decay time 160_{-35}^{+45} d, with residuals of rms 0.076 km s^{-1} . The period derived from the GPR on our raw RVs is shorter than the

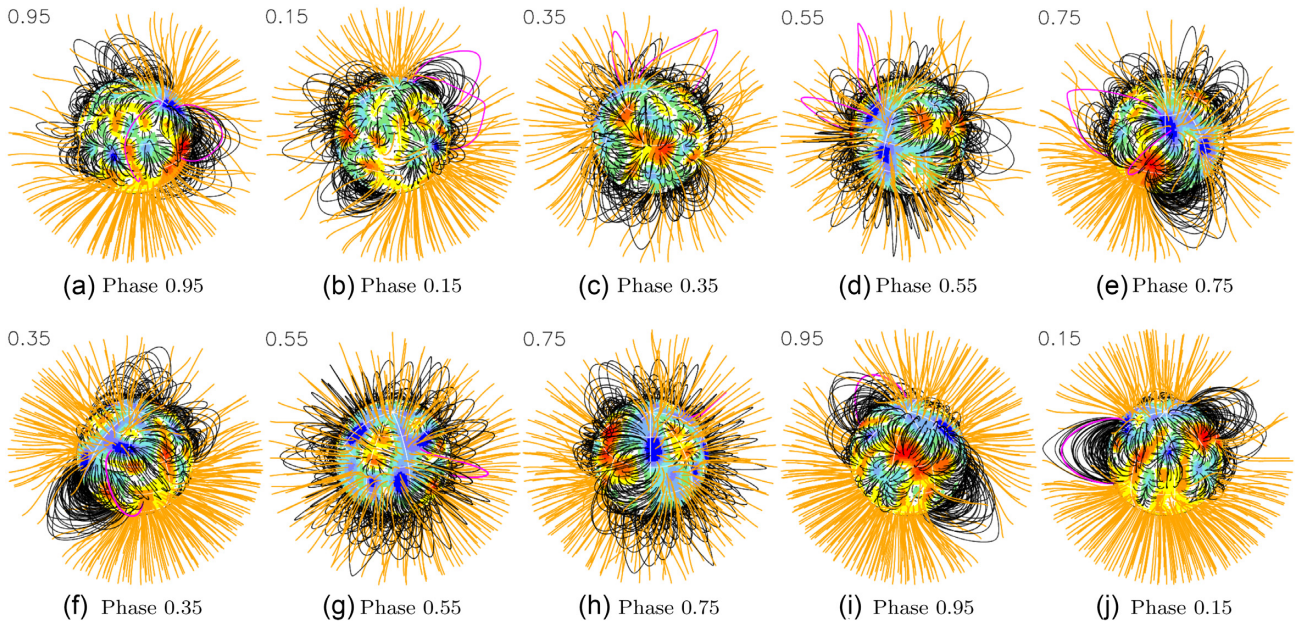


Figure 14. Potential field extrapolations of the ZDI-reconstructed surface radial field, as seen by an Earth-based observer, for observation epochs 2009 Jan (top) and 2011 Jan (bottom) at different phases. Open/closed field lines are shown in orange/black, respectively, and colours at the stellar surface depict the local value of the radial field (in G, as shown in the left-hand panels of Fig. 3). The source surface at which field lines open is set to $2.18 R_*$. The field lines that would carry the potential observed prominences (phases 0.95 and 0.8 in 2009, phase 0.35 in 2011) are coloured in magenta. Animated versions with the star rotating are available at <http://userpages.irap.omp.eu/lyu/jan09a.gif> and <http://userpages.irap.omp.eu/lyu/jan11n.gif>.

period we used to phase our data, and corresponds to a latitude of 5.5° . This period is much closer to the period derived with GPR from B_ℓ than to the period derived from $H\alpha$, showing that in this case, B_ℓ is a better activity proxy than $H\alpha$ (for a more systematic study of the correlation of B_ℓ with stellar activity, see Hébrard et al. 2016). The decay time associated with RVs is much shorter than the differential rotation lap time and the decay times of the V magnitude, $H\alpha$, and B_ℓ (see Table 6), which suggests that RVs are more sensitive to small-scale short-lived features while the photometry, $H\alpha$, and B_ℓ are more sensitive to large-scale long-lasting features.

Through both processes, the residual RVs present no significant periodicity which would betray the presence of a potential planet. To estimate the planet mass detection threshold, GPR–MCMC was run on simulated data sets, composed of a base activity jitter (our GP model from Section 5), and a circular planet signature, plus a white noise of level 0.081 km s^{-1} . Various planet separations and masses were tested, and for each case, GPR–MCMC was run several times with different randomization seeds, to mitigate statistical bias. For every randomization seed, GPR–MCMC was run with a model including a planet and a model including no planet, and the difference of logarithmic marginal likelihood between them (hereafter $\Delta\mathcal{L}$) was computed. Finally, the detection threshold was set at $\Delta\mathcal{L} = 10$ and the minimum detectable mass at each separation was interpolated from the mass/ $\Delta\mathcal{L}$ curve. Fig. 17 shows the planet mass detection threshold as a function of planet–star separation: we thus obtained a detectability threshold of $\sim 1 M_{\text{Jup}}$ for $a < 0.09$ au and $\sim 4.6 M_{\text{Jup}}$ for $a = 0.15$ au. The figure also shows the parameters of V830 Tau b and TAP 26 b, showing that we would likely have detected a planet like TAP 26 b but not one like V830 Tau b. Planets beyond $a = 0.15$ au are difficult to detect due to the temporal coverage of our data, that never exceeds 19 d at any given epoch. The early depletion of the disc may have prevented the formation and/or the migration of giant exoplanets. Kraus et al. (2016) outlines

a correlation between the presence of a close companion and a lack of planets, in a sample of binary stars with mass ratios $q > 0.4$, which could support the hypothesis that V410 Tau B, although having a slightly lower mass ratio ($q = 0.2 \pm 0.1$, Kraus et al. 2011), played a role in the early disc dissipation, which in turn prevented the formation of a hot Jupiter.

In terms of methodology, GPR fits the data down to a significantly lower χ_r^2 than ZDI because it is capable of accounting for most of the mid-term variability, contrarily to ZDI, which for now only integrates differential rotation and a simplistic description of intrinsic variability. Small structures evolve on time-scales of \sim few weeks, so we need to be able to model their temporal evolution in a more elaborate way to be able to match the capability of GPR to fit time-variable RV curves. Self-consistent methods that combine the physical faithfulness of ZDI and the flexibility of GPR will be developed in the near future and applied to more MaTYSSSE data, as well as to data from the SPIRou (Spectropolarimetre InfraRouge) Legacy Survey (SLS). Finally, observing V410 Tau and other wTTSs with SPIRou will yield spectra in the near-infrared, where we expect a smaller jitter than in the optical bandwidth, and will offer an opportunity to benchmark our activity jitter filtering technique performances.

ACKNOWLEDGEMENTS

This paper is based on observations obtained at the Canada–France–Hawaii Telescope (CFHT), operated by the National Research Council of Canada, the Institut National des Sciences de l’Univers of the Centre National de la Recherche Scientifique (INSU/CNRS) of France and the University of Hawaii, and at the T el escope Bernard Lyot (TBL), operated by Observatoire Midi-Pyr enes and by INSU/CNRS. We thank the Queued Service Observations (QSO) teams of CFHT and TBL for their great work and efforts at collecting the high-quality MaTYSSSE (Magnetic Topologies of Young Stars

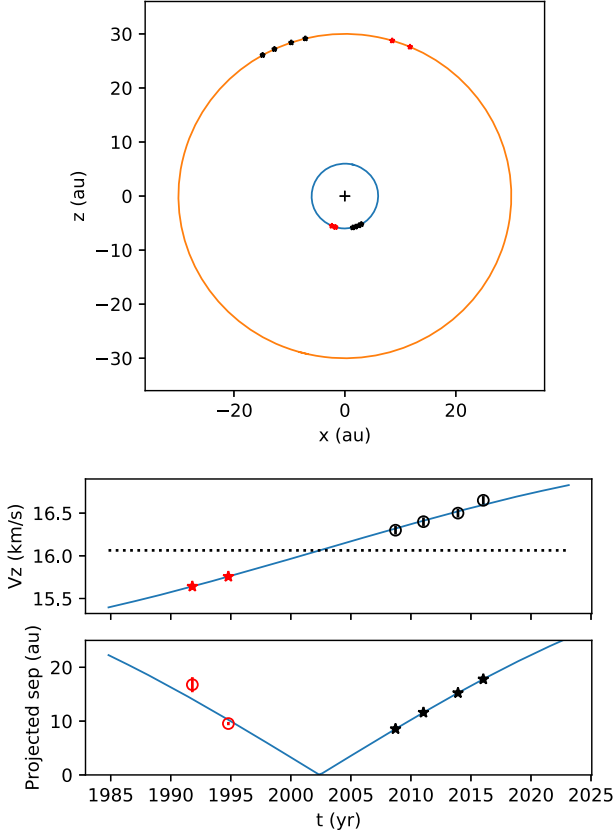


Figure 15. Circular model for the binary motion of V410 Tau A and V410 Tau B: edge-on orbit, separation 36.0 au, period 166 a and systemic radial velocity 16.06 km s^{-1} . *Top*: top view of the model orbit, with the z -axis parallel to the line of sight, where the positions of V410 Tau A and B according to the model are marked by red and black stars at the times of the separation measurements and of our spectropolarimetric seasons (2008b–2009a, 2011a, 2013b, and 2015b–2016a) respectively. *Middle*: RV_{bulk} of V410 Tau A with time, as measured by us in black dots with 1σ error bars and as derived from the model orbit in blue. The predicted RV_{bulk} at the times of the separation measurements are represented by red stars. *Bottom*: Sky-projected binary separation as a function of time, as measured by Ghez et al. (1995) in red dots with 1σ error bars, and as derived from the model orbit in blue. The predicted sky-projected separations at the dates of our observing seasons are marked in black stars.

and the Survival of close-in massive Exoplanets) data presented here, without which this study would not have been possible. MaTYSSSE is an international collaborative research programme involving experts from more than 10 different countries (France, Canada, Brazil, Taiwan, United Kingdom, Russia, Chile, United States of America, Ireland, Switzerland, Portugal, China, and Italy).

JFD also warmly thanks the Initiative d’Excellence (IDEX) at Université Fédérale Toulouse Midi-Pyrénées (UFTMiP) for funding the STEPS collaboration program between the Institut de Recherche en Astrophysique et Planétologie at the Observatoire Midi-Pyrénées (IRAP/OMP) and the European Southern Observatory (ESO). JFD acknowledges funding from the European Research Council (ERC) under the H2020 research & innovation programme (grant agreements 740651 New Worlds). We acknowledge funding from the Laboratoire d’Excellence (LabEx) OSUG@2020 (Observatoire des Sciences de l’Univers de Grenoble) that allowed purchasing the ProLine PL230 CCD imaging system installed on the 1.25 m telescope at the Crimean Astrophysical Observatory.

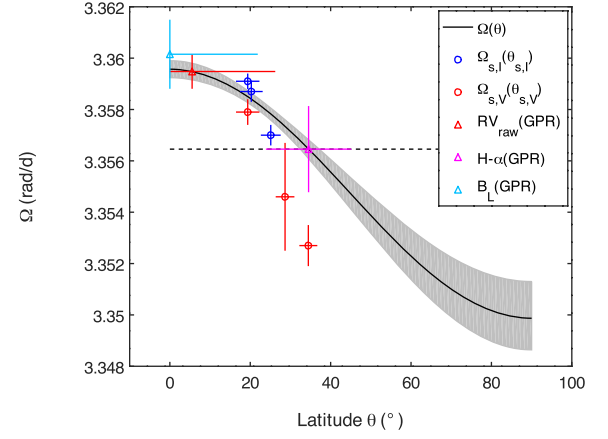


Figure 16. Differential rotation curve of V410 Tau (black full line) with 1σ uncertainty in grey, with $\Omega_{\text{eq}} = 3.35957 \pm 0.00006 \text{ rad d}^{-1}$ and $d\Omega = 0.0097 \pm 0.0003 \text{ rad d}^{-1}$. The stellar rotation rate chosen to phase our data is represented as a dashed horizontal line. The rotation rates derived from the RVs (red), from the $H\alpha$ EWs (magenta), and from the longitudinal field measurements (cyan) are positioned on the differential rotation curve as triangles with 1σ error bars, thus yielding the barycentric latitude of the features determining the period. The dots represent barycentric couples $\{90 - \theta_s, \Omega_s\}$ derived in our epoch-wise differential rotation measurements, those coming from Stokes I / Stokes V data being plotted in blue / red, respectively.

Table 6. Various evolution time-scales.

Quantity	Time-scale (d)
RV decay time	160^{+45}_{-35}
V mag decay time	314^{+31}_{-29}
$H\alpha$ decay time	589^{+774}_{-335}
B_L decay time	604^{+553}_{-289}
Differential rotation lap time	648 ± 73

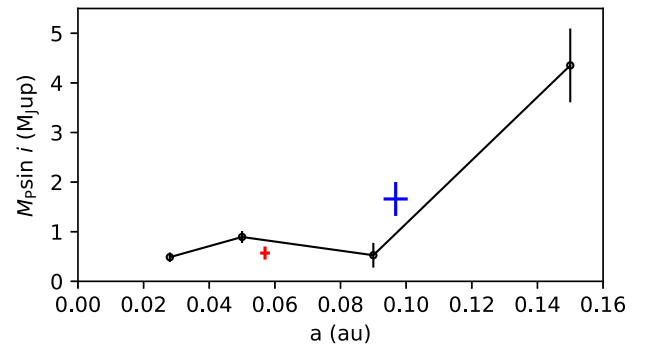


Figure 17. Detectability threshold in terms of $M_p \sin i$ for planets at various a , with the RV filtering technique involving GPR. V830 Tau b is plotted in red (parameters from Donati et al. 2017) and TAP 26 b in blue (parameters from Yu et al. 2017).

Finally, we warmly thank the referee for taking the time to review this research.

This research has made use of the SIMBAD data base, operated at CDS, Strasbourg, France, and of the Matplotlib python module (Hunter 2007).

REFERENCES

- Baraffe I., Homeier D., Allard F., Chabrier G., 2015, *A&A*, 577, A42
- Bouvier J., 2007, in Bouvier J., Appenzeller I., eds, Proc. IAU Symp. 243, Star-Disk Interaction in Young Stars. Kluwer, Dordrecht, p. 231
- Bouvier J., Alencar S. H. P., Harries T. J., Johns-Krull C. M., Romanova M. M., 2007, in Reipurth B., Jewitt D., Keil K., eds, Protostars and Planets V. University of Arizona Press, Tucson, p. 479
- Bouvier J., Bertout C., 1989, *A&A*, 211, 99
- Carroll T. A., Strassmeier K. G., Rice J. B., Künstler A., 2012, *A&A*, 548, A95
- Collier Cameron A., Woods J. A., 1992, *MNRAS*, 258, 360
- Donati J.-F., Brown S. F., 1997, *A&A*, 326, 1135
- Donati J.-F., Collier Cameron A., Petit P., 2003, *MNRAS*, 345, 1187
- Donati J.-F., Landstreet J. D., 2009, *ARA&A*, 47, 333
- Donati J.-F., Mengel M., Carter B. D., Marsden S., Collier Cameron A., Wichmann R., 2000, *MNRAS*, 316, 699
- Donati J.-F., Semel M., Carter B. D., Rees D. E., Collier Cameron A., 1997, *MNRAS*, 291, 658
- Donati J.-F. et al., 2006, *MNRAS*, 370, 629
- Donati J.-F. et al., 2007, *MNRAS*, 380, 1297
- Donati J.-F. et al., 2008, *MNRAS*, 386, 1234
- Donati J.-F. et al., 2010a, *MNRAS*, 402, 1426
- Donati J.-F. et al., 2010b, *MNRAS*, 409, 1347
- Donati J.-F. et al., 2011, *MNRAS*, 412, 2454
- Donati J.-F. et al., 2012, *MNRAS*, 425, 2948
- Donati J.-F. et al., 2013, *MNRAS*, 436, 881
- Donati J.-F. et al., 2014, *MNRAS*, 444, 3220
- Donati J.-F. et al., 2015, *MNRAS*, 453, 3706
- Donati J.-F. et al., 2017, *MNRAS*, 465, 3343
- Donati J. F. et al., 2016, *Nature*, 534, 662
- Galli P. A. B. et al., 2018, *ApJ*, 859, 33
- Ghez A. M., Weinberger A. J., Neugebauer G., Matthews K., McCarthy D. W. Jr, 1995, *AJ*, 110, 753
- Ghez A. M., White R. J., Simon M., 1997, *ApJ*, 490, 353
- Grankin K. N., Bouvier J., Herbst W., Melnikov S. Y., 2008, *A&A*, 479, 827
- Gregory S. G., Donati J.-F., Morin J., Hussain G. A. J., Mayne N. J., Hillenbrand L. A., Jardine M., 2012, *ApJ*, 755, 97
- Gully-Santiago M. A. et al., 2017, *ApJ*, 836, 200
- Hambálek Ā., Vařko M., Paunzen E., Smalley B., 2019, *MNRAS*, 483, 1642
- Haywood R. D. et al., 2014, *MNRAS*, 443, 2517
- Haywood R. D. et al., 2016, *MNRAS*, 457, 3637
- Hunter J. D., 2007, *Computing in Science & Engineering*, 9, 90
- Hussain G. A. J. et al., 2009, *MNRAS*, 398, 189
- Hébrard É. M., Donati J.-F., Delfosse X., Morin J., Moutou C., Boisse I., 2016, *MNRAS*, 461, 1465
- Johns-Krull C. M., Valenti J. A., Koresko C., 1999, *ApJ*, 516, 900
- Kraus A. L., Ireland M. J., Hillenbrand L. A., Martinache F., 2012, *ApJ*, 745, 19
- Kraus A. L., Ireland M. J., Huber D., Mann A. W., Dupuy T. J., 2016, *AJ*, 152, 8
- Kraus A. L., Ireland M. J., Martinache F., Hillenbrand L. A., 2011, *ApJ*, 731, 8
- Kurucz R., 1993, CDROM # 13 (ATLAS9 atmospheric models) and # 18 (ATLAS9 and SYNTHE routines, spectral line database). Smithsonian Astrophysical Observatory, Washington DC
- Landi degl'Innocenti E., Landolfi M., 2004, *Polarisation in Spectral Lines*. Kluwer Academic Publishers, Dordrecht
- Luhman K. L., Allen P. R., Espaillat C., Hartmann L., Calvet N., 2010, *ApJS*, 186, 111
- Meunier N., Desort M., Lagrange A.-M., 2010, *A&A*, 512, A39
- Morin J. et al., 2008, *MNRAS*, 390, 567
- Moutou C. et al., 2007, *A&A*, 473, 651
- Pecaut M. J., Mamajek E. E., 2013, *ApJS*, 208, 9
- Pollacco D. L. et al., 2006, *PASP*, 118, 1407
- Rice J. B., Strassmeier K. G., Kopf M., 2011, *ApJ*, 728, 69
- Siess L., Dufour E., Forestini M., 2000, *A&A*, 358, 593
- Skelly M. B., Donati J.-F., Bouvier J., Grankin K. N., Unruh Y. C., Artemenko S. A., Petrov P., 2010, *MNRAS*, 403, 159
- Sokoloff D. D., Nefedov S. N., Ermash A. A., Lamzin S. A., 2008, *Astron. Lett.*, 34, 761
- Stelzer B. et al., 2003, *A&A*, 411, 517
- Vaytet N., Commerçon B., Masson J., González M., Chabrier G., 2018, *A&A*, 615, A5
- Welty A. D., Ramsey L. W., 1995, *AJ*, 110, 336
- Yadav R. K., Christensen U. R., Morin J., Gastine T., Reiners A., Poppenhaefer K., Wolk S. J., 2015, *ApJ*, 813, L31
- Yu L. et al., 2017, *MNRAS*, 467, 1342

SUPPORTING INFORMATION

Supplementary data are available at [MNRAS](https://academic.oup.com/mnras/article/489/4/5556/5561492) online.

Appendix A. Observations.

Appendix B. Photometry Analysis.

Appendix C. Activity Proxies.

Please note: Oxford University Press is not responsible for the content or functionality of any supporting materials supplied by the authors. Any queries (other than missing material) should be directed to the corresponding author for the article.

This paper has been typeset from a $\text{\TeX/L\AA}^{\text{A}}\text{\TeX}$ file prepared by the author.